Research paper

Mechanics of mutable hierarchical composite cellular materials

F. Ongaro[a], E. Barbieri[*,b], N.M. Pugno[*,a,c,d]

[a] School of Engineering and Materials Science, Queen Mary University of London, London, UK
[b] Japan Agency for Marine-Earth Science and Technology (JAMSTEC), Department of Mathematical Science and Advanced Technology (MAT), Yokohama Institute for Earth Sciences (YES), 3173-25, Showa-machi, Kanazawa-ku Yokohama-city, Kanagawa, 236-0001, Japan
[c] Laboratory of Bio-Inspired and Graphene Nanomechanics, Department of Civil, Environmental and Mechanical Engineering, University of Trento, Trento, Italy
[d] Ket-Lab, Edoardo Amaldi Foundation, Italian Space Agency, Via del Politecnico snc, Rome, Italy

ABSTRACT

Cellular structures having the internal volumes of the cells filled with fluids, fibres or other bulk materials are very common in nature. A remarkable example of composite solution is the hygroscopic keel tissue of the ice plant *Delosperma nakurense*. This tissue, specialized in promoting the mechanism for seed dispersal, reveals a cellular structure composed by elongated cells filled with a cellulosic swelling material. Upon hydrating, the filler adsorbs large amounts of water leading to a change in the cells' shape and effective stiffness.

This paper, inspired by the configuration of the aforementioned hygroscopic keel tissue, deals with the analysis of a two-dimensional honeycomb made of elongated hexagonal cells filled with an elastic material. The system is treated as a sequence of Euler–Bernoulli beams on Winkler foundation, whose displacements are derived by introducing the classical shape functions of the Finite Element Method. The assumption of the Born rule, in conjunction with an energy-based approach, provide the constitutive model in the continuum form. It emerges a strong influence of the infill's stiffness and cell walls' inclination on the macroscopic elastic constants. In particular, parametric analysis reveals the system isotropy only in the particular case of regular hexagonal microstructure.

Even though a rigorous analysis of the keel tissue is well beyond our aim, the application of the theoretical model to estimate the effective stiffness of such biological system leads to results that are in good agreement with the published data, where the keel tissue is represented as an internally pressurized honeycomb. Specifically, an energetic equivalence gives an explicit relation between the inner pressure and the filler's stiffness. Optimal values of pressure and cell walls' inclination also emerge.

Finally, the theory is extended to the hierarchical configuration and a closed form expression for the macroscopic elastic moduli is provided. It emerges a synergy of hierarchy and material heterogeneity in obtaining a stiffer material, in addition to an optimal number of hierarchical levels.

1. Introduction

Cellular materials are commonly observed in nature (Gibson et al., 2010; Meyers et al., 2008; Altenbach and Oechsner, 2010; Gibson and Ashby, 2001; Gibson, 2012). Due to their specific structural properties, they are very promising for engineering applications in a variety of industries including aerospace, automotive, marine and constructions (Wilson, 1990; Thompson and Matthews, 1995; Bitzer, 1994). As an example, honeycombs are widely used in lightweight structures and sandwich panels because of their high bending stiffness and strength at low weight.

Many authors extensively studied cellular materials and it would be difficult to quote without omissions the vast literature flourished on the mechanical modelling of such cellular structures in the last years. Noteworthy contributions such as Gibson and Ashby (2001), Gibson (1989) and Gibson et al. (1982) present a detailed discussion of the characteristics of many periodic cellular materials and provide simple relations between their density and equivalent mechanical properties through the application of beam theory. Other authors, like Ongaro et al. (2016b), Davini and Ongaro (2011), Kumar and McDowell (2004), Burgardt and Cartraud (1999) and Chen et al. (1998) suggest alternative approaches to solve the crucial passage from discrete to continuum and to derive the constitutive model for the in-plane deformation of various two-dimensional microstructures by applying

the energy equivalence. In addition, Warren and Byskov (2002), Wang and Stronge (1999), Dos Reis and Ganghoffer (2012) and Dos Reis and Ganghoffer (2010) exploit a method based on the principles of structural analysis to obtain the homogenized continuum model of the discrete lattice.

Although many efforts have been devoted to the prediction of the effective properties of regular cellular materials with empty cells, in the literature few investigations concern the characterisation of cellular structures having the internal volumes filled with fluids, fibres or other bulk materials as commonly happens in nature (Georget et al., 2003; Niklas, 1992; 1989; Van Liedekerke et al., 2010; Warner et al., 2000; Wu and Pitts, 1999; Zhu and Melrose, 2003; Mihai et al., 2015). For example, in the context of sandwich panels, D'Mello and Waas (2013) and Burlayenko and Sadowski (2010) present a finite element-based technique to evaluate the structural performance of foam filled honeycombs. It emerges an increase in the load-bearing capacity of the material and an improvement in both the effective elastic properties and energy absorption due to the presence of the filler. More recently, Ongaro et al. (2016b) analyses the mechanics of a two-dimensional filled honeycomb by representing the microstructure as a sequence of beams on Winkler elastic foundation. The homogenized elastic moduli derived confirm, from a mechanical behaviour point of view, the beneficial effect due to the filling material. Other works, Harrington et al. (2011) and Guiducci et al. (2014), concerning the nature's wonders of design, study the mechanics of the hygroscopic keel tissue of the ice plant *Delosperma nakurense* (Fig. 1) by representing it as a network of elongated cells internally pressurized. The ice plant, that grows in the arid regions of Africa, is a source of inspiration because of its sophisticated origami-like movement mechanism for seed dispersal. The plant, in particular, has adopted its anatomy and material architecture to the unfavourable environmental conditions by producing a special seed capsule to prevent the premature dispersion of the seeds. In the dry state, Fig. 1, five petal-like sections, the protective valves, cover the seed compartment as a box-like lid. When it rains, the valves unfold backwards revealing a seed compartment composed by five seed chambers partitioned by five septa, Fig. 1. Within few minutes, most of the seeds are splashed out by the falling water (Lockyer, 1932). When the capsule dries up, the valves return to the original position. The specialized organ promoting this movement is the hygroscopic keel, Fig. 1. In the dry state, this tissue consists of a network of elongated cells filled with a 'swelling cellulosic inner' (CIL). If hydrated, the CIL absorbs large amounts of water giving rise to a change of the keel initial geometry and stiffness, Fig. 1. In addition, experimental observations (Harrington et al., 2011) reveal that the filler contains a soft inclusion that behaves like an elongated, thin septum partitioning the internal volume of the cell. Consequently, the cell walls' coupling effect due to the presence of the filling material is compromised. Though many studies experimentally investigated the morphology and composition of the keel, little is known about the relation between microstructure's parameters and macroscopic mechanical behaviour (Guiducci et al., 2014).

Hierarchy is another way to enhance the mechanical properties of lightweight materials and structures.

Various authors studied structural hierarchy in biological systems (Gibson, 2012; Fratzl and Weinkamer, 2007; Mattheck and Kubler, 1995; Pan, 2014; Gao, 2010; Chen and Pugno, 2013) and man-made materials (Barthelat and Mirkhalaf, 2013; Sanchez et al., 2005; Fratzl, 2007). Among others, Pugno and Chen (2011), Haghpanah et al. (2014), Ajdari et al. (2012), Fan et al. (2008) and Taylor et al. (2011) provide numerical and theoretical models, force or energy based, to understand the role of hierarchy on the mechanical behaviour of cellular solids. All of them conclude that many desirable properties, like stress attenuation, superplasticity, and increased toughness, are due to hierarchy. Conversely, for classical cellular materials, the introduction of some levels of hierarchy is detrimental for the specific stiffness. In spite of this, in the case of hierarchical architectures of different types of fibre bundles, increasing the number of hierarchical levels leads to an improvement in the material strength (Bosia et al., 2012).

Inspired by the previously introduced hygroscopic keel tissue, this paper deals with a two-dimensional composite cellular material made of elongated hexagonal cells, filled with an elastic medium. The study provides a theoretical model, based on the Born rule, that is able to understand the mechanics of the examined orthotropic configuration and is general enough to investigate the effects of adding some levels of hierarchy. This work is organised in 6 sections, including this introduction. Section 2 initially illustrates the mathematical formulation and modelling technique while, in Section 3, the effective elastic constants and constitutive equations are derived. Some considerations about the influence of the microstructure parameters, such as the stiffness of the filler and the cell walls' inclination, are presented in Section 4, as well as the results of the application of the theoretical model to the biological keel tissue. Despite a detailed investigation of the biological problem is beyond our scope, it emerges that the elastic moduli obtained in this paper agree with those proposed in the literature. Finally, in Section 5, the theory is extended to the hierarchical configuration and explicit expressions for the macroscopic elastic moduli are derived. As a conclusion, Section 6 summarizes the main findings.

2. Problem statement: geometrical description and theoretical modelling of the discrete system

2.1. Geometrical description

In terms of crystallography, the configuration of the composite material considered here can be described as the union of two simply shifted lattices (Fig. 2(a))

$$L_1(\ell) = \{\mathbf{x} \in \mathbb{R}^2 : \mathbf{x} = n^1 \mathbf{l}_1 + n^2 \mathbf{l}_2, \text{ with } (n^1, n^2) \in \mathbb{Z}^2\}, \quad L_2(\ell)$$
$$= \mathbf{s} + L_1(\ell), \tag{1}$$

with

$$\mathbf{l}_1 = (2\ell\cos\theta, \ 0), \quad \mathbf{l}_2 = (\ell\cos\theta, \ \ell(1 + \sin\theta)) \tag{2}$$

the lattice vectors,

$$\mathbf{s} = (\ell\cos\theta, \ \ell\sin\theta) \tag{3}$$
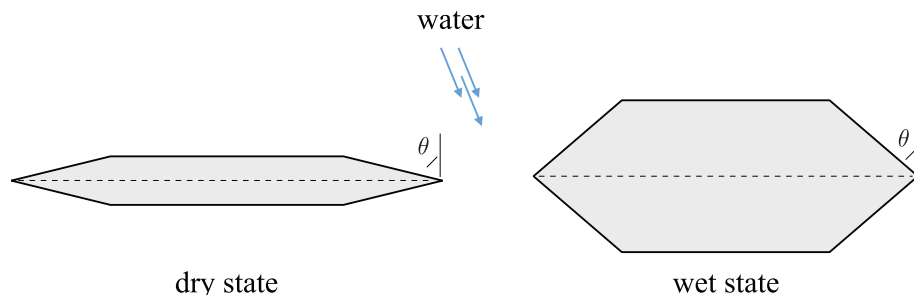
water

dry state
wet state

Fig. 1. A schematic representation of the hygroscopic keel tissue of the ice plant *Delosperma nakurense*.
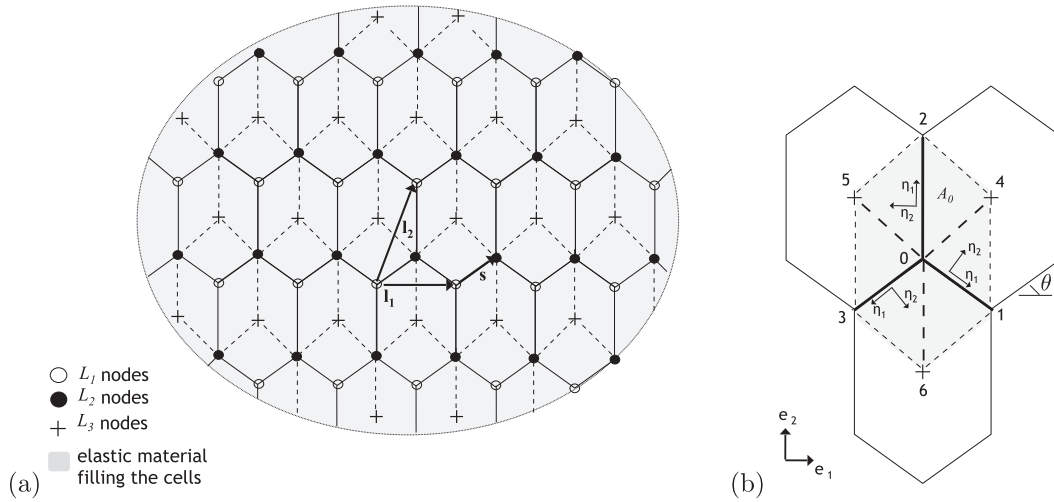
Fig. 2. Theoretical modelling of the composite hexagonal microstructure: (a) geometrical modelling, (b) the unit cell.

the shift vector, ℓ and θ, respectively, the length (the lattice size) and angle of inclination of the cell walls.

2.2. Theoretical modelling

2.2.1. The discrete system continuum-springs

The discrete system is treated as a sequence of Euler–Bernoulli beams on Winkler foundation, where a series of independent, linear elastic springs, the Winkler foundation, represent the material within the cells. In particular, each beam is supported by two sets of springs: the springs a, in the $-\eta_2^e$ direction, and the springs b, in the η_2^e (Fig. 3).

Being a rigorous analysis of the biological keel tissue a complex undertaking that does not coincide with the scope of our investigation, in the present paper the missing cell walls' coupling effect caused by the septum is modelled by anchoring the springs at the nodes of the lattice L_3, defined by

$$L_3(\ell) = 2\mathbf{s} + L_1(\ell). \tag{4}$$

As illustrated in Fig. 2(a), the nodes of L_3 are connected to the lattice L_2 by means of line elements that, from a mechanical point of view, are represented as Euler–Bernoulli beams having stiffness much smaller than the stiffness of the cell walls. Consequently, the energetic contribution of the beams composing the lattice L_3 can be neglected with respect to those composing the skeleton of the cells (i.e., the principal lattices L_1 and L_2), introduced in the following section.

With reference to the equilibrium conditions of the springs' anchorage points it should be noted that the forces brought by the springs to such nodes balance with one another because of the symmetry of the hexagonal cells.
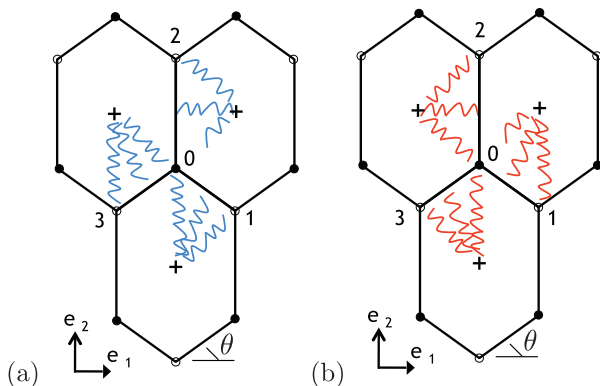
In particular, let us focus on the hexagonal cell illustrated in Fig. 4, where each beam is connected to the central point of the cell by closely-spaced elastic springs (i.e., the Winkler foundation). Note that, for ease of reading, in Fig. 4 the series of closely spaced springs are schematically represented by a single spring connecting the beams to the central point of the cell. As it can be seen, the symmetry of the hexagonal cell leads to a symmetric configuration of the springs. To make it more clear, in Fig. 5 the two sets of symmetric springs (i.e., the springs a represented in blue and the springs b represented in red) are enhanced. Let us now imagine to apply external forces to the cell, leading to a generic deformation of the cell. Again, because of the symmetry of both the hexagonal cell and the configuration of the springs, it emerges that, in terms of anchorage points (i.e., the central point of the cell), the forces brought by the springs balance with one another. Further details are provided in Section 2.4.

2.2.2. The Euler–Bernoulli beam on Winkler foundation element

In the two-dimensional Euler–Bernoulli beam, each node has three degrees of freedom, two translations and one rotation. Thus, the vector of nodal displacements can be expressed as

$$\mathbf{u}^e = [\mathbf{u}_i \ \mathbf{u}_j]^T = [u_i \ v_i \ \varphi_i \ u_j \ v_j \ \varphi_j]^T. \tag{5}$$

According to the Finite Element Method (FEM), the axial and transverse displacements at every point within the beam are approximated by

$$\begin{bmatrix} u(x) \\ v(x) \end{bmatrix} = \mathbf{\Psi}(x)\mathbf{u}^e, \tag{6}$$

with $(0 \le x \le \ell)$ and

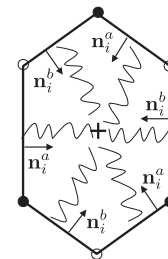**Fig. 3.** The discrete system continuum-springs: (a) springs a, (b) springs b.

Fig. 4. The anisotropic hexagonal cell in the Winkler model with focus on the springs' anchorage point.
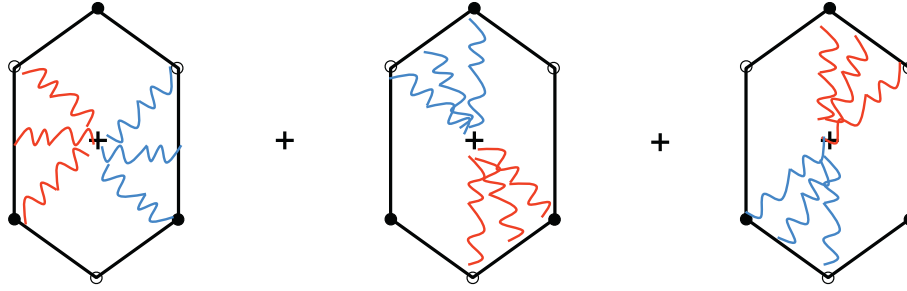
Fig. 5. Equilibrium of the forces at the springs' anchorage point: the two sets of symmetric springs (springs *a* represented in red, springs *b* represented in blue). (For interpretation of the references to colour in this figure legend, the reader is referred to the web version of this article.)

$$
\Psi(x) = \begin{bmatrix} \Psi_1(x) & 0 & 0 & \Psi_4(x) & 0 & 0 \\ 0 & \Psi_2(x) & \Psi_3(x) & 0 & \Psi_5(x) & \Psi_6(x) \end{bmatrix} \tag{7}
$$

is the shape functions matrix, whose components are

$$
\Psi_1(x) = 1 - \frac{x}{\ell}, \quad \Psi_2(x) = 1 - 3\left(\frac{x}{\ell}\right)^2 + 2\left(\frac{x}{\ell}\right)^3, \quad \Psi_3(x) = \left(\frac{x}{\ell} - 2\left(\frac{x}{\ell}\right)^2 + \left(\frac{x}{\ell}\right)^3\right)\ell,
$$

$$
\Psi_4(x) = \frac{x}{\ell}, \qquad \Psi_5(x) = 3\left(\frac{x}{\ell}\right)^2 - 2\left(\frac{x}{\ell}\right)^3, \qquad \Psi_6(x) = \left(\left(\frac{x}{\ell}\right)^2 + \left(\frac{x}{\ell}\right)^3\right)\ell. \tag{8}
$$

The elastic strain energy of the Euler–Bernoulli beam on Winkler foundation element can be evaluated as the sum of three terms (Ongaro et al., 2016b; Dinev, 2012):

$$
w^e = \frac{1}{2}(\mathbf{u}^e)^T \cdot \mathbf{k}_b^e \mathbf{u}^e + \frac{1}{2}(\Delta\mathbf{u}^{e,a})^T \cdot \mathbf{k}_{wf}^e \Delta\mathbf{u}^{e,a} + \frac{1}{2}(\Delta\mathbf{u}^{e,b})^T \cdot \mathbf{k}_{wf}^e \Delta\mathbf{u}^{e,b}. \tag{9}
$$

The first is the elastic energy due to the axial and bending deformations of the beam, the second and third are related to the elongation of the springs,

$$
\Delta\mathbf{u}^{e,a} = [\Delta\mathbf{u}_i^a \; \Delta\mathbf{u}_j^a]^T, \tag{10}
$$

$$
\Delta\mathbf{u}^{e,b} = [\Delta\mathbf{u}_i^b \; \Delta\mathbf{u}_j^b]^T. \tag{11}
$$

In particular, for the beams 0–1, 0–2 and 0–3, the quantities in (10) and (11) are, respectively,

$$
\Delta\mathbf{u}_1^a = \begin{bmatrix} \mathbf{u}_0 - \mathbf{u}_6 \\ \mathbf{u}_1 - \mathbf{u}_6 \end{bmatrix}, \quad \Delta\mathbf{u}_1^b = \begin{bmatrix} \mathbf{u}_0 - \mathbf{u}_4 \\ \mathbf{u}_1 - \mathbf{u}_4 \end{bmatrix}, \tag{12}
$$

$$
\Delta\mathbf{u}_2^a = \begin{bmatrix} \mathbf{u}_0 - \mathbf{u}_4 \\ \mathbf{u}_2 - \mathbf{u}_4 \end{bmatrix}, \quad \Delta\mathbf{u}_2^b = \begin{bmatrix} \mathbf{u}_0 - \mathbf{u}_5 \\ \mathbf{u}_2 - \mathbf{u}_5 \end{bmatrix}, \tag{13}
$$

$$
\Delta\mathbf{u}_3^a = \begin{bmatrix} \mathbf{u}_0 - \mathbf{u}_5 \\ \mathbf{u}_3 - \mathbf{u}_5 \end{bmatrix}, \quad \Delta\mathbf{u}_3^b = \begin{bmatrix} \mathbf{u}_0 - \mathbf{u}_6 \\ \mathbf{u}_3 - \mathbf{u}_6 \end{bmatrix}. \tag{14}
$$

Finally, with obvious notation, $\mathbf{k}_b^e$ and $\mathbf{k}_{wf}^e$, in turn, stand for the stiffness matrix of the classical Euler–Bernoulli beam and of the Winkler foundation. In the FEM framework, their components are obtained by applying the strain energy principle (Tsiatas, 2014). In particular,

$$
[\mathbf{k}_b^e]_{ij} = \begin{cases} \int_0^\ell C_\ell \Psi_i'(x)\Psi_j'(x)\,dx, & i,j = 1, 4, \\ \int_0^\ell D_\ell \Psi_i''(x)\Psi_j''(x)\,dx, & i,j = 2, 3, 5, 6, \\ 0, & \text{otherwise} \end{cases} \tag{15}
$$

and

$$
[\mathbf{k}_{wf}^e]_{ij} = \begin{cases} \int_0^\ell K_w \Psi_i(x)\Psi_j(x)\,dx, & i,j = 2, 3, 5, 6, \\ 0, & \text{otherwise}, \end{cases} \tag{16}
$$

with K_w the Winkler foundation constant, $C_\ell = \frac{E_s h}{1 - \nu_s^2}$ and $D_\ell = \frac{E_s h^3}{12(1 - \nu_s^2)}$, respectively, the tensile and bending stiffness (per unit width) of the beams, E_s, ν_s, h, ℓ, in turn, Young's modulus, Poisson's ratio, thickness, and length of the beams, while $(\cdot)' = \frac{\partial(\cdot)}{\partial x}$ and $(\cdot)'' = \frac{\partial^2(\cdot)}{\partial x^2}$. Substituting (8) into (15) and (16) leads to

$$
\mathbf{k}_b^e = \begin{bmatrix} C_\ell/\ell & 0 & 0 & -C_\ell/\ell & 0 & 0 \\ 0 & 12D_\ell/\ell^3 & 6D_\ell/\ell^2 & 0 & -12D_\ell/\ell^3 & 6D_\ell/\ell^2 \\ 0 & 6D_\ell/\ell^2 & 4D_\ell/\ell & 0 & -6D_\ell/\ell^2 & 2D_\ell/\ell \\ -C_\ell/\ell & 0 & 0 & C_\ell/\ell & 0 & 0 \\ 0 & -12D_\ell/\ell^3 & -6D_\ell/\ell^2 & 0 & 12D_\ell/\ell^3 & -6D_\ell/\ell^2 \\ 0 & 6D_\ell/\ell^2 & 2D_\ell/\ell & 0 & -6D_\ell/\ell^2 & 4D_\ell/\ell \end{bmatrix} \tag{17}
$$

and

$$
\mathbf{k}_{wf}^e = \begin{bmatrix} 0 & 0 & 0 & 0 & 0 & 0 \\ 0 & 13K_w/35 & 11K_w\ell/210 & 0 & 9K_w/70 & -13K_w\ell/420 \\ 0 & 11K_w\ell/210 & K_w\ell^2/105 & 0 & 13K_w\ell/420 & -K_w\ell^2/140 \\ 0 & 0 & 0 & 0 & 0 & 0 \\ 0 & 9K_w/70 & 13K_w\ell/420 & 0 & 13K_w/35 & -11K_w\ell/210 \\ 0 & -13K_w\ell/420 & -K_w\ell^2/140 & 0 & -11K_w\ell/210 & K_w\ell^2/105 \end{bmatrix}. \tag{18}
$$

It should be noted that there are different approaches in evaluating the stiffness matrix of beam elements on elastic foundations (Tsiatas, 2014). The two main techniques are based on either the use of approximated shape functions (Janco, 2010; Kuo and Lee, 1994; Hosur and Bhavikatti, 1996; Chen, 1998) or the development of exact ones (Eisenberger and Yankelevsky, 1985; Sen et al., 1990; Razaqpur and Shah, 1991). In the first case, both $\mathbf{k}_b^e$ and $\mathbf{k}_{wf}^e$ are evaluated by adopting the cubic polynomial shape functions typical of the Euler–Bernoulli beam, listed in (8). In the second, the shape functions are derived by solving the governing differential equation of the Euler–Bernoulli beam resting on Winkler foundation (Eisenberger and Yankelevsky, 1985). However, despite the simplifications introduced, several existing studies dealing with a broad range of engineering problems (Janco, 2010; Tsiatas, 2014; Karkon and Karkon, 2016) conclude that the results of the numerical implementations based on the approximated solution compare favourably to those obtained by the exact ones. Considering this and aiming to obtain a more mathematically tractable problem, in this work the approximated approach is

adopted (cf. Eq. (16)).

2.3. Elastic energy of the discrete system

For any given deformation, the elastic energy representative of the whole discrete structure, W, can be evaluated from the analysis of the unit cell of the periodic array.

As illustrated in Fig. 2(b), the unit cell is composed by the central node 0 and the external nodes 1, 2, 3, 4, 5, 6, linked by the line elements 0–1, 0–2, 0–3, treated as Euler–Bernoulli beams on Winkler foundation, and 0–4, 0–5, 0–6, modelled as Euler–Bernoulli beams. In the global reference system ($\mathbf{e}_1$, $\mathbf{e}_2$), the beams are represented, respectively, by the vectors

$$\mathbf{b}_1 = \mathbf{l}_1 - \mathbf{s}, \quad \mathbf{b}_2 = \mathbf{l}_2 - \mathbf{s}, \quad \mathbf{b}_3 = -\mathbf{s}, \quad \mathbf{b}_4 = \mathbf{s}, \quad \mathbf{b}_5 = -\mathbf{l}_1 - \mathbf{s}, \quad \mathbf{b}_6$$
$$= (\mathbf{s} - \mathbf{l}_2)/2. \tag{19}$$

The elastic energy W, in particular, is obtained by summing the elastic energies of the beams. However, as stated in Section 2.2.1, the contribution of the beams composing the lattice L_3, 0–4, 0–5, 0–6, is assumed to be negligible with respect to those composing the principal lattices L_1 and L_2, 0–1, 0–2, 0–3. Consequently, in evaluating W, only the beams 0–1, 0–2, 0–3 will be considered.

Furthermore, as it can be seen in Fig. 2(b), the first node of each beam coincides with the central node 0, where it is imposed the balance of forces and moments. This condition guarantees the equilibrium of the examined cell and allows us to condense the degrees of freedom of 0, leading to

$$W = W(\mathbf{u}_j, \Delta\mathbf{u}_j^a, \Delta\mathbf{u}_j^b), \qquad j = 1, 2, 3, \tag{20}$$

with

$$\Delta\mathbf{u}_1^a = [\mathbf{u}_1 - \mathbf{u}_6], \quad \Delta\mathbf{u}_1^b = [\mathbf{u}_1 - \mathbf{u}_4], \tag{21}$$

$$\Delta\mathbf{u}_2^a = [\mathbf{u}_2 - \mathbf{u}_4], \quad \Delta\mathbf{u}_2^b = [\mathbf{u}_2 - \mathbf{u}_5], \tag{22}$$

$$\Delta\mathbf{u}_3^a = [\mathbf{u}_3 - \mathbf{u}_5], \quad \Delta\mathbf{u}_3^b = [\mathbf{u}_3 - \mathbf{u}_6]. \tag{23}$$

2.4. Discussion

According to our method, it emerges that the elastic energy of the discrete system is given by (cf. Eq. (20))

$$W = W(\mathbf{u}_j, \Delta\mathbf{u}_j^a, \Delta\mathbf{u}_j^b), \qquad j = 1, 2, 3. \tag{24}$$

In particular, the energetic contribution due to the Winkler foundation,

$$W_{Winkler} = W_{Winkler}(\Delta\mathbf{u}_j^a, \Delta\mathbf{u}_j^b), \qquad j = 1, 2, 3, \tag{25}$$

is a quadratic function of the elongation of the springs involving, as stated, the difference between the displacements of the end points of the beams and of the anchorage points. As it can be seen, the displacements of the nodes 4, 5 and 6 does not "directly" take part in the description of the system; they only contribute via the terms $\Delta\mathbf{u}_j^a$ and $\Delta\mathbf{u}_j^b$.

This can be verified by imagining to represent the composite architecture in Fig. 2(a) as an hybrid system composed by one-dimensional (1D) beams and two-dimensional (2D) filler. With reference to the unit cell in Fig. 2(b), the elastic energy of the hybrid 1D-2D configuration is the sum of the elastic energies of the beams, W_{beams}, and of the filler, W_{filler}:

$$W_{1D-2D} = W_{beams} + W_{filler}. \tag{26}$$

W_{filler}, in particular, is given by

$$W_{filler} = \frac{1}{2} \int_V \boldsymbol{\varepsilon}_f^T \, \boldsymbol{\sigma}_f \, dV, \tag{27}$$

with

$$\boldsymbol{\varepsilon}_f := \begin{bmatrix} \varepsilon_{11} \\ \varepsilon_{22} \\ 2\varepsilon_{12} \end{bmatrix} \leftarrow \begin{bmatrix} \varepsilon_{11} & \varepsilon_{12} \\ \varepsilon_{12} & \varepsilon_{22} \end{bmatrix} = : \boldsymbol{\epsilon}_f \tag{28}$$

and

$$\boldsymbol{\sigma}_f := \begin{bmatrix} \sigma_{11} \\ \sigma_{22} \\ \sigma_{12} \end{bmatrix} \leftarrow \begin{bmatrix} \sigma_{11} & \sigma_{12} \\ \sigma_{12} & \sigma_{22} \end{bmatrix} = : \mathbf{T}_f, \tag{29}$$

respectively, the infinitesimal strain tensor, $\boldsymbol{\epsilon}_f$, and stress tensor, $\mathbf{T}_f$, expressed in Voigt notation, $\mathbf{C}_f$ the stiffness tensor of the material within the cell, satisfying the generalised Hooke's law

$$\boldsymbol{\sigma}_f = \mathbf{C}_f \boldsymbol{\varepsilon}_f. \tag{30}$$

For two-dimensional isotropic materials in plane-stress tensional state, $\mathbf{C}_f$ is defined by

$$\mathbf{C}_f := \frac{E_f}{1 - \nu_f^2} \begin{bmatrix} 1 & \nu_f & 0 \\ \nu_f & 1 & 0 \\ 0 & 0 & (1 - \nu_f)/2 \end{bmatrix}, \tag{31}$$

with E_f and ν_f, in turn, Young's modulus and Poisson's ratio of the filler.

Accordingly, by substituting (30) into (27) and considering a unitary width, $b = 1$, it emerges

$$W_{filler} = \frac{1}{2} \int_{A_0} \boldsymbol{\varepsilon}_f^T \, \mathbf{C}_f \boldsymbol{\varepsilon}_f \, dA, \tag{32}$$

being $V = bA_0$ and A_0 the area of the examined cell (Fig. 2(b)).

By discretizing the area A_0 into a set of two-dimensional triangular elements having nodes

$$\begin{aligned}
&0 - 1 - 4, \\
&0 - 4 - 2, \\
&0 - 2 - 5, \\
&0 - 5 - 3, \\
&0 - 3 - 6, \\
&0 - 6 - 1
\end{aligned} \tag{33}$$

and by considering the so-called constant-strain triangular element (CST) frequently used in the Finite Element Method, (32) takes the form

$$W_{filler} = \sum_{e=1}^6 \frac{1}{2} \mathbf{d}_e^T \mathbf{k}_e \mathbf{d}_e, \tag{34}$$

with $\mathbf{k}_e$ and $\mathbf{d}_e = [\mathbf{u}_i \, \mathbf{u}_j \, \mathbf{u}_m]^T$, respectively, the local stiffness matrix and displacements vector of each triangular element of nodes i, j and m (Fenner, 1996). Specifically,

$$\begin{aligned}
\mathbf{d}_{0-1-4} &= [\mathbf{u}_0 \, \mathbf{u}_1 \, \mathbf{u}_4]^T, \\
\mathbf{d}_{0-4-2} &= [\mathbf{u}_0 \, \mathbf{u}_4 \, \mathbf{u}_2]^T, \\
\mathbf{d}_{0-2-5} &= [\mathbf{u}_0 \, \mathbf{u}_2 \, \mathbf{u}_5]^T, \\
\mathbf{d}_{0-5-3} &= [\mathbf{u}_0 \, \mathbf{u}_5 \, \mathbf{u}_3]^T, \\
\mathbf{d}_{0-3-6} &= [\mathbf{u}_0 \, \mathbf{u}_3 \, \mathbf{u}_6]^T, \\
\mathbf{d}_{0-6-1} &= [\mathbf{u}_0 \, \mathbf{u}_6 \, \mathbf{u}_1]^T
\end{aligned} \tag{35}$$

provide the displacements vector of the examined triangles.

In terms of the global displacements vector, $\mathbf{D}$, and stiffness matrix, $\mathbf{K}$, obtained by "summing" their local counterparts, (34) becomes

$$W_{filler} = \frac{1}{2} \mathbf{D}^T \mathbf{K} \mathbf{D} = \frac{1}{2} \begin{bmatrix} \mathbf{u}_0 \\ \mathbf{u}_1 \\ \mathbf{u}_2 \\ \mathbf{u}_3 \\ \mathbf{u}_4 \\ \mathbf{u}_5 \\ \mathbf{u}_6 \end{bmatrix}^T \mathbf{K} \begin{bmatrix} \mathbf{u}_0 \\ \mathbf{u}_1 \\ \mathbf{u}_2 \\ \mathbf{u}_3 \\ \mathbf{u}_4 \\ \mathbf{u}_5 \\ \mathbf{u}_6 \end{bmatrix} \tag{36}$$

or, by splitting the vector $\mathbf{D}$ into the vectors $\mathbf{D}_1 = [\mathbf{u}_0 \, \mathbf{u}_1 \, \mathbf{u}_2 \, \mathbf{u}_3]^T$ and $\mathbf{D}_2 = [\mathbf{u}_4 \, \mathbf{u}_5 \, \mathbf{u}_6]^T$ that, with reference to our model, represent the displacements of the principal lattices, L_1 and L_2, and of the central points

of the cells (i.e., the springs' anchorage points),

$$W_{filler} = \frac{1}{2}\begin{bmatrix} \mathbf{D}_1 \\ \mathbf{D}_2 \end{bmatrix}^T \begin{bmatrix} \mathbf{K}_{11} & \mathbf{K}_{12} \\ \mathbf{K}_{21} & \mathbf{K}_{22} \end{bmatrix} \begin{bmatrix} \mathbf{D}_1 \\ \mathbf{D}_2 \end{bmatrix}, \tag{37}$$

leading to

$$W_{filler} = \frac{1}{2}(\mathbf{D}_1^T\mathbf{K}_{11}\mathbf{D}_1 + \mathbf{D}_1^T\mathbf{K}_{12}\mathbf{D}_2 + \mathbf{D}_2^T\mathbf{K}_{21}\mathbf{D}_1 + \mathbf{D}_2^T\mathbf{K}_{22}\mathbf{D}_2), \tag{38}$$

with $\mathbf{K}_{ij}$ obtained by partitioning $\mathbf{K}$.

When $\nu_f = 1/3$, value that coincides with Poisson's ratio of the hygroscopic keel tissue considered in the present paper, it emerges that the elastic energy in (38) can be expressed as a quadratic function of the quantities $\mathbf{u}_i - \mathbf{u}_j$, with $i = 0, 1, 2, 3$ and $j = 4, 5, 6$. Specifically,

$$W_{filler} = W_{filler}(\mathbf{u}_0 - \mathbf{u}_k, \mathbf{u}_1 - \mathbf{u}_l, \mathbf{u}_2 - \mathbf{u}_m, \mathbf{u}_3 - \mathbf{u}_n), \tag{39}$$

where $k = 4, 5, 6$, $l = 6, 4, 5$, $m = 4, 5$ and $n = 5, 6$.

As it can be seen, similarly to (25), in Eq. (39) the displacements of the nodes 4, 5, 6 are not "directly" involved in the description of the system; their contribution is only related to the terms $\mathbf{u}_i - \mathbf{u}_j$ that, in the Winkler model, represent the elongation of the springs.

Also, by assuming that the elastic energy of the beams is the same in the two considered models (i.e., hybrid system 1D–2D and Winkler model), it can be concluded that, in the case of $\nu_f = 1/3$,

$$W_{filler} = \frac{1}{2}(\mathbf{D}_1^T\mathbf{K}_{11}\mathbf{D}_1 + \mathbf{D}_1^T\mathbf{K}_{12}\mathbf{D}_2 + \mathbf{D}_2^T\mathbf{K}_{21}\mathbf{D}_1 + \mathbf{D}_2^T\mathbf{K}_{22}\mathbf{D}_2)$$

$$\sim W_{Winkler} = \sum_e \frac{1}{2}((\Delta\mathbf{u}^{e,a})^T \cdot \mathbf{k}_{wf}^e \Delta\mathbf{u}^{e,a} + (\Delta\mathbf{u}^{e,b})^T \cdot \mathbf{k}_{wf}^e \Delta\mathbf{u}^{e,b}). \tag{40}$$

A final observation concerns the equilibrium conditions of the springs' anchorage points, i.e., the nodes 4, 5 and 6 (Fig. 2(b)).

As mentioned in Section 2.2.1, the symmetry of both the hexagonal cell and the configuration of the springs provide the equilibrium of the forces at the springs' anchorages. This geometrically-based consideration can be verified by considering the equivalence between the hybrid system 1D beams-2D filler and the system Euler–Bernoulli beams on Winkler foundation described above. In particular, when the hexagonal cell in Fig. 4 is subjected to a set of external forces leading to a generic deformation of the cell, the reaction forces of the springs along the direction $\mathbf{n}_i$ take the form

$$\mathbf{f}_i = (\mathbf{n}_i^T\mathbf{K}_w\mathbf{n}_i)\Delta u_i \mathbf{n}_i, \tag{41}$$

where $\mathbf{K}_w$ is the stiffness matrix of the elastic foundation and Δu_i the elongation of the springs in the $\mathbf{n}_i$ direction.

At the anchorage points (i.e., the central point of the cell), the sum of the springs' reaction forces is expressed by

$$\mathbf{f}_{anc} = \sum \mathbf{f}_i = \sum (\mathbf{n}_i^T\mathbf{K}_w\mathbf{n}_i)\Delta u_i \mathbf{n}_i \tag{42}$$

or, by splitting the contribution of the two sets of springs,

$$\mathbf{f}_{anc} = \sum ((\mathbf{n}_i^a)^T\mathbf{K}_w\mathbf{n}_i^a)\Delta u_i^a \mathbf{n}_i^a + \sum ((\mathbf{n}_i^b)^T\mathbf{K}_w\mathbf{n}_i^b)\Delta u_i^b \mathbf{n}_i^b, \tag{43}$$

with Δu_i^a and Δu_i^b, respectively, the elongation of the springs a and of the springs b in the directions $\mathbf{n}_i^a$ and $\mathbf{n}_i^b$ (Fig. 4).

By taking into account the equivalence between the system 1D beams-2D filler and the Winkler model, it can be assumed

$$\Delta u_i = \Delta d_i, \tag{44}$$

being Δu_i and Δd_i, respectively, the elongation in the $\mathbf{n}_i$ direction in the Winkler foundation model and in the system 1D beams-2D filler. From classical continuum mechanics,

$$\Delta d_i = (\mathbf{n}_i^T\epsilon_f\mathbf{n}_i)d_i \tag{45}$$

with d_i the original length of the cell in the $\mathbf{n}_i$ direction and ϵ_f the infinitesimal strain tensor (cf. Eq. (28)).

By substituting (44) into (42) and splitting the contribution of the

springs a and of the springs b as in Eq. (43), it emerges

$$\mathbf{f}_{anc} = \sum ((\mathbf{n}_i^a)^T\mathbf{K}_w\mathbf{n}_i^a)((\mathbf{n}_i^a)^T\epsilon_f\mathbf{n}_i^a)d_i^a \mathbf{n}_i^a$$

$$+ \sum ((\mathbf{n}_i^b)^T\mathbf{K}_w\mathbf{n}_i^b)((\mathbf{n}_i^b)^T\epsilon_f\mathbf{n}_i^b)d_i^b \mathbf{n}_i^b. \tag{46}$$

Finally, by observing that $d_i^a = d_i^b$ and that $\mathbf{n}_i^a = -\mathbf{n}_i^b$, Eq. (46) provides

$$\mathbf{f}_{anc} = \mathbf{0}, \tag{47}$$

relation that coincides with the equilibrium of the forces at the springs, anchorage points. It should be noted that the above equation is valid for any deformation of the cell, both symmetric and not-symmetric.

3. The homogenized model

3.1. Elastic energy

It is possible to express W in a continuum form by introducing the affine interpolants of the nodal displacements and microrotations, $\hat{\mathbf{u}}(\cdot)$ and $\hat{\varphi}(\cdot)$, and by assuming that in the limit $\ell \to 0$ the discrete variables $(\mathbf{u}_j, \varphi_j)$ previously introduced can be expressed by

$$\mathbf{u}_j = \hat{\mathbf{u}}_0 + \nabla\hat{\mathbf{u}}\,\mathbf{b}_j, \qquad \varphi_j = \hat{\varphi}_0 + \nabla\hat{\varphi}\,\mathbf{b}_j, \qquad j = 1, 2, 3. \tag{48}$$

The terms $\hat{\mathbf{u}}_0$ and $\hat{\varphi}_0$ stand for the values of $\hat{\mathbf{u}}(\cdot)$ and $\hat{\varphi}(\cdot)$ at the central node of the cell in the continuum description, while $\mathbf{b}_j$ are the vectors formerly defined. Substituting (48) into (20) and dividing the expression that turns out from the calculation by the area of the unit cell, $A_0 = 2\ell^2\cos\theta(1 + \sin\theta)$ (Fig. 2(b)), give the strain energy density in the continuum approximation w. Similarly to Ongaro et al. (2016b) and Davini and Ongaro (2011), in the limit $\ell \to 0$ it emerges the independency of w by the microrotation gradients, $\hat{\varphi}_{,\alpha}$, that scale with first order in ℓ. Accordingly,

$$w = w(\varepsilon_{11}, \varepsilon_{22}, \varepsilon_{12}, (\omega - \hat{\varphi})), \tag{49}$$

with $\varepsilon_{\alpha\beta} = \frac{1}{2}(\hat{u}_{\alpha,\beta} + \hat{u}_{\beta,\alpha})$ and $\omega = \frac{1}{2}(\hat{u}_{1,2} - \hat{u}_{2,1})$ the infinitesimal strains and the infinitesimal rotation of classical continuum mechanics. More details are given in Appendices A and B.

3.2. Constitutive equations

The stress–strain relations of the equivalent continuum take the form

$$\sigma_{11} = \frac{\begin{aligned}&C_\ell c(\varepsilon_{11}(24c^4D_\ell + c^2(C_\ell\ell^2 + 48D_\ell s^2)) + s(\varepsilon_{22}(C_\ell\ell^2 - 12D_\ell)f_0\\&+ \varepsilon_{11}(12D_\ell s(1 + 2s^2))))\end{aligned}}{\ell f_0(24c^2D_\ell + C_\ell\ell^2(1 + 2s^2))} + $$
$$+ \frac{K_w c(\varepsilon_{11}f_1 - \varepsilon_{22}f_2)}{104f_0f_3},$$

$$\sigma_{22} = \frac{C_\ell(C_\ell\varepsilon_{22}\ell^2s^2f_0 + c^2(\varepsilon_{11}(C_\ell\ell^2 s - 12D_\ell s) + 12D_\ell\varepsilon_{22}f_0))}{c\ell(24c^2D_\ell + C_\ell\ell^2(1 + 2s^2))}$$
$$+ \frac{K_w(\varepsilon_{22}f_4/c - \varepsilon_{11}cf_2)}{104f_0f_3},$$

$$\sigma_{12}^{sym} = \sigma_{21}^{sym} = \frac{3D_\ell\varepsilon_{12}(c^2(C_\ell\ell^2(4\,sf_0(s^2 + s + 3) + 3) - 24D_\ell sf_0))}{2\ell^3f_0c(2C_\ell\ell^2c^2 + 3D_\ell(4\,sf_0 + 3))}$$
$$+ \frac{3D_\ell\varepsilon_{12}(4c^4(C_\ell\ell^2(2\,sf_0 + 1) + 3D_\ell) + 4C_\ell\ell^2c^6 + 12D_\ell s^2f_0^2)}{2\ell^3f_0c(2C_\ell\ell^2c^2 + 3D_\ell(4\,sf_0 + 3))}$$
$$+ \frac{K_w\varepsilon_{12}f_5}{208cf_0f_3},$$

$$\sigma_{12}^{skw} = -\sigma_{21}^{skw} = \frac{9D_\ell(\omega - \hat{\varphi})}{c\ell^3(3 + 4sf_0)},$$

$$\sigma_{12} = \sigma_{12}^{sym} + \sigma_{12}^{skw}, \quad \sigma_{21} = \sigma_{21}^{sym} + \sigma_{21}^{skw},$$
$$\tag{50}$$

with $\sigma_{\gamma\delta}^{sym}$ and $\sigma_{\gamma\delta}^{skw}$, in turn, the symmetric and skew-symmetric part of

the Cauchy stress tensor defined by

$$\sigma = \frac{1}{A_0} \frac{\partial W}{\partial \nabla \hat{\mathbf{u}}}.$$

(51)

Note that, to simplify the notation, in (50) c and s stand, respectively, for $\cos\theta$ and $\sin\theta$ while $f_i = f_i(\cos\theta, \sin\theta)$ are polynomial expressions listed in Appendix B.

3.3. Elastic constants

Mathematical manipulations provide the elastic constants of the limit problem, given by

$$E_1^* = \frac{c(K_w \nu c^2((4\lambda^3 f_8 E_s)/\nu + f_6 K_w(2s^2+1)) + 4\lambda E_s((104\lambda^3 E_s f_{10})/(\nu f_0) + f_7 K_w))}{4(f_9 K_w \nu(2\lambda^2 c^2 + 2s^2 + 1) + 104\lambda f_{10} E_s(\lambda^2 c^2 + s^2))}$$
$$+ \frac{\lambda^2 K_w^2 f_6 \nu c^5}{2(f_9 K_w \nu(2\lambda^2 c^2 + 2s^2 + 1) + 104\lambda f_{10} E_s(\lambda^2 c^2 + s^2))},$$

$$\nu_{12}^* = -\frac{c^2(K_w \nu f_2(2\lambda^2 c^2 + 2s^2 + 1) + 104\lambda(\lambda^2 - 1)E_s f_{11})}{K_w \nu f_4(2\lambda^2 c^2 + 2s^2 + 1) + 104\lambda f_0 E_s(\lambda^2 c^2 + s^2)f_{11}/s},$$

$$E_2^* = \frac{4E_s((104\lambda^3 E_s f_{10})/(\nu f_0) + f_7 K_w) + K_w c^2(4\lambda^3 E_s f_8 + K_w \nu f_6(2s^2 + 1))}{4f_0 c(K_w \nu f_1(2\lambda^2 c^2 + 2s^2 + 1) + 104\lambda^3 f_3 E_s(s^2(3 + 2c^2) + 2c^4 + c^2))}$$
$$+ \frac{\lambda^2 K_w^2 \nu c^3 f_6}{2f_0(K_w \nu f_1(2\lambda^2 c^2 + 2s^2 + 1) + 104\lambda^3 f_3 E_s(s^2(3 + 2c^2) + 2c^4 + c^2))},$$

$$\nu_{21}^* = -\frac{K_w \nu f_2(2\lambda^2 c^2 + 2s^2 + 1) + 104\lambda(\lambda^2 - 1)f_{11}E_s}{K_w \nu f_1(2\lambda^2 c^2 + 2s^2 + 1) + 104\lambda^3 E_s f_3(s^2(3 + 2c^2) + 2c^4 + c^2)},$$

$$G^* = \frac{1}{416 f_0 c}\left(\frac{104\lambda^3 E_s(c^2(2\lambda^2 + f_{13}) - 2\lambda^2 s f_0 + f_{12})}{\nu(\lambda^2(4f_0 s + 3) + 8c^2)} + \frac{K_w f_{11}}{f_{10}}\right),$$

(52)

with $\lambda = h/\ell$, $\nu = (1 - \nu_s^2)$, $c = \cos\theta$, $s = \sin\theta$ and $f_i = f_i(\cos\theta, \sin\theta)$ the expressions in Appendix B. Also, with obvious notation, E_1^*, ν_{12}^* and E_2^*, ν_{21}^* denote, in turn, Young's modulus and the corresponding Poisson's ratio in the $\mathbf{e}_1$ and $\mathbf{e}_2$ direction, G^* the shear modulus. As expected, the macroscopic elastic moduli derived satisfy the classical relation revealing the system isotropy, $G^* = \frac{E^*}{2(1 + \nu^*)}$, with $E_1^* = E_2^* \equiv E^*$ and $\nu_{12}^* = \nu_{21}^* \equiv \nu^*$, only in the particular case $\theta = 30°$.

4. Discussion

4.1. The hygroscopic keel tissue: Comparison with other authors

As stated, the present work is inspired by the hygroscopic keel tissue of the ice plant. This biological tissue reveals a cellular microstructure composed by elongated hexagons filled with the CIL. If hydrated, the CIL adsorbs large amount of water, leading to a change of the cells' shape and, consequently, to the macroscopic stiffness.

As a matter of fact, let us consider the compact expression of the stress–strain relations derived in Section 3.2

$$\begin{bmatrix} \sigma_{11}^{sym} \\ \sigma_{22}^{sym} \\ \sigma_{12}^{sym} \end{bmatrix} = \begin{bmatrix} C_{11} & C_{12} & C_{13} \\ C_{21} & C_{22} & C_{23} \\ C_{31} & C_{32} & C_{33} \end{bmatrix} \begin{bmatrix} \varepsilon_{11} \\ \varepsilon_{22} \\ 2\varepsilon_{12} \end{bmatrix},$$

(53)

with C_{ij} the components of the effective stiffness tensor previously obtained and reported here for ease of reading

$$C_{11} = \frac{C_\ell c(24c^4 D_\ell + c^2(C_\ell \ell^2 + 48D_\ell s^2) + s(12D_\ell s(1 + 2s^2)))}{\ell f_0(24c^2 D_\ell + C_\ell \ell^2(1 + 2s^2))}$$
$$+ \frac{K_w c f_1}{104 f_0 f_3},$$

$$C_{22} = \frac{C_\ell(C_\ell \ell^2 s^2 + 12D_\ell c^2)f_0}{c\ell(24c^2 D_\ell + C_\ell \ell^2(1 + 2s^2))} + \frac{K_w f_4/c}{104 f_0 f_3},$$

$$C_{12} = C_{21} = \frac{C_\ell cs(C_\ell \ell^2 - 12D_\ell)}{\ell(24c^2 D_\ell + C_\ell \ell^2(1 + 2s^2))} - \frac{K_w c f_2}{104 f_0 f_3},$$

$$C_{33} = \frac{3D_\ell c(C_\ell \ell^2(4 s f_0(s^2 + s + 3) + 3) - 24D_\ell s f_0)}{2\ell^3 f_0 c(2C_\ell \ell^2 c^2 + 3D_\ell(4 s f_0 + 3))}$$
$$+ \frac{3D_\ell(4c^4(C_\ell \ell^2(2 s f_0 + 1) + 3D_\ell) + 4C_\ell \ell^2 c^6 + 12D_\ell s^2 f_0^2)}{2\ell^3 f_0 c(2C_\ell \ell^2 c^2 + 3D_\ell(4 s f_0 + 3))}$$
$$+ \frac{K_w f_5}{208 c f_0 f_3},$$

$$C_{13} = C_{23} = C_{31} = C_{32} = 0.$$

(54)

It emerges a strong influence of the inclination of the cell walls θ (Fig. 2), via the terms $c = \cos\theta$, $s = \sin\theta$ and the polynomials $f_i = f_i(\cos\theta, \sin\theta)$.

Before addressing a parametric analysis to investigate further this influence, let us verify the adopted modelling technique by comparing the proposed results with the available data in the literature.

As summarised in Table 1, the comparison is established by comparing the C_{ij} constants of the present paper with those suggested in Guiducci et al. (2014), where the keel tissue, represented as a pressurized diamond-shaped honeycomb, is analyzed by Finite Element homogenization and theoretical modelling based on the Born rule. Specifically, four cell configurations are considered, characterised by different values of θ and inner pressure, p. Notwithstanding the diverse strategies adopted, Table 1 reveals that the agreement is generally good. The discrepancies that emerge in some cases are due to the different cells' shape considered: diamond-shaped cells in Guiducci et al. (2014), elongated hexagons in the present work. Also, neglecting the compromised cell walls' coupling effect could be another
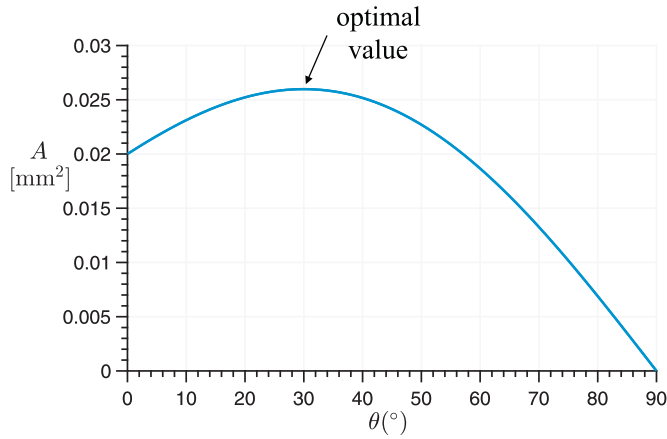
Table 1
A practical application to the keel tissue of the ice plant. Comparison between the results of the present paper and those of Guiducci et al. (2014).

	Guiducci et al. (2014)				
	$E_s = 1$ GPa,	$\nu_s = 0.3$,	$h/\ell = 0.07$		
p (MPa)	C_{22} (GPa)	C_{11} (GPa)	C_{33} (GPa)	C_{12} (GPa)	C_{21} (GPa)
0	0.1 ÷ 0.3	0.002	0.004 ÷ 0.012	0.028	0.028
2.5	0.03	0.020 ÷ 0.027	0.03 ÷ 0.086	0.020 ÷ 0.026	0.023 ÷ 0.026
5	0.025	0.03 ÷ 0.05	0.03 ÷ 0.086	0.015	0.015
6	0.02	0.03 ÷ 0.04	0.02 ÷ 0.096	0.02	0.02
			Present		
	$E_s = 1$ GPa,	$\nu_s = 0.3$,	$h/\ell = 0.07$		
$\theta(°)$	K_w (MPa)	C_{22} (GPa)	C_{11} (GPa)	C_{33} (GPa)	C_{12} (GPa)	C_{21} (GPa)
75	0	0.15	0.002	0.0035	0.025	0.025
48	15.27	0.020	0.020	0.04	0.018	0.018
47	33	0.019	0.046	0.057	0.018	0.018
46	41.1	0.02	0.05	0.054	0.016	0.016

Fig. 6. Optimal value of θ, with $\ell = 1$ mm: area of the cell.

source of dissimilarities. As mentioned in Section 2.1, a rigorous analysis of the biological keel tissue is beyond our aim. However, from Table 1 it emerges that the proposed theory could be applied in biology to study the mechanics of composite tissues having a not-regular hexagonal microstructure.

In addition, in Table 1 the values of the Winkler foundation constant, K_w, are obtained by the energetic equivalence described in Appendix C. In particular, it emerges that K_w, expressed by

$$K_w(p) = \frac{\sqrt{2}\, p\left(-\dfrac{8\sin\theta\cos\theta}{17} + 1\right)\cos\theta\sqrt{1 + \sin\theta}}{\left(\dfrac{4\sin^3\theta}{6+\sqrt{2}} + \dfrac{4\cos^3\theta}{6-\sqrt{2}} - 1\right)^2 + \cos\theta\left(\dfrac{4\cos\theta}{6-\sqrt{2}} - 1\right)^2},$$

(55)

is a function of the pressure, p, and cell walls' inclination, $\theta = \theta(p)$.

One question that arises is if there exist an optimal value of p, $\tilde{p}$, that maximises the area of the hexagonal cell, A_0, given by

$$A_0(p) = 2\ell^2 \cos\theta(p)\cdot(1 + \sin\theta(p)),$$

(56)

with ℓ and $\theta(p)$, in turn, the length and inclination of the cell walls.

As illustrated in Fig. 6, A_0 attains the maximum at $\theta \equiv \tilde{\theta} = 30°$ and, according to the analysis of Guiducci et al. (2014), the corresponding value of p is given by $\tilde{p} \approx 15$ MPa. It should be noted that the outcome of the analysis is not affected by the particular value of cell walls' length

assumed in Fig. 6, $\ell = 1$ mm.

Finally, a schematic representation of this smart mechanism is shown in Fig. 7. In the dry state, at zero pressure, the tissue is composed by elongated cells characterised by high values of θ and minimum absorption (Fig. 7(a)). When it starts raining, the filler absorbs more and more large amounts of water, leading to an increase in the inner pressure and, consequently, to a decrease in θ. In particular, decreasing θ provides an increase in A_0 (cf. Fig. 6), as well as an increase in the absorption (Fig. 7(b)). At $\theta = 30°$, the stationary condition of maximum absorption is reached (Fig. 7(c)). Then, when the rain stops, the pressure inside the cells decreases, as the absorbed water starts to evaporate (Fig. 7(d)). It follows an increase in θ and a decrease in A_0, until the original configuration is restored (Fig. 7(e)).

4.2. Parametric analysis

From the expressions in (54) it is clear that the macroscopic mechanical behaviour is strongly affected by the microstructure's geometrical and mechanical properties.

Assuming lignified cell walls as in the keel tissue, with $E_s = 1$ GPa and $\nu_s = 0.3$ (Guiducci et al., 2014), this section investigates the influence of the infill's stiffness, K_w, and cell walls' inclination, θ, in the effective stiffness. In particular, two different cases are considered: slender beams, with $h/\ell = 0.01$, Fig. 8, and thick beams, with $h/\ell = 0.1$, Fig. 9. As it can be seen, Figs. 8(a) and 9(a) suggest that when K_w is fixed, an increase in θ leads to a decrease in the C_{11} constant, that is more significant in the case of $h/\ell = 0.1$ (Fig. 9(a)). Conversely, for fixed K_w, increasing the cell walls' inclination provides an increase in C_{22} (Figs. 8(b) and 9(b)). This is not surprising since the smaller the angle θ, the more elongated in the $\mathbf{e}_1$ direction will be the resulting cell. Consequently, the smaller θ, the higher C_{11}. Similarly, increasing θ yields a more and more elongated cell in the $\mathbf{e}_2$ direction and a more and more higher C_{22}. In addition, Figs. 8(a), 9(a) and 8(b), 9(b) show that, for fixed θ, to high values of $K_w(10^{-1}E_s, 10^{-2}E_s)$ corresponds an higher initial value of both C_{11} and C_{22}.

Regarding the constant C_{33}, from Figs. 8(e) and 9(e) it emerges that when K_w is fixed, an increase in θ leads to an increase in C_{33}, that is more evident for high values of $K_w(10^{-1}E_s, 10^{-2}E_s)$.

In terms of the cross stiffness components, C_{12} and C_{21}, Figs. 8(c), 9(c) and 8(d), 9(d) reveal that increasing θ provides a fast initial increase followed by a gradual decrease. In contrast to what would be
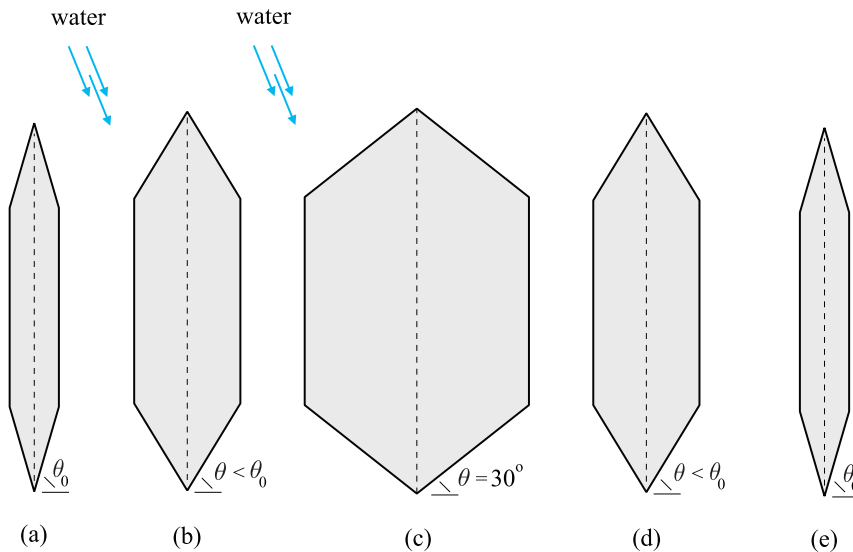

Fig. 7. The smart mechanism of the hygroscopic keel tissue: (a) dry state, (b) when it starts raining, the filler absorbs water leading to an increase in the absorption capability, (c) stationary condition, maximum absorption, (d) the rain stops and the water absorbed starts to evaporate, until (e) the original configuration is restored.
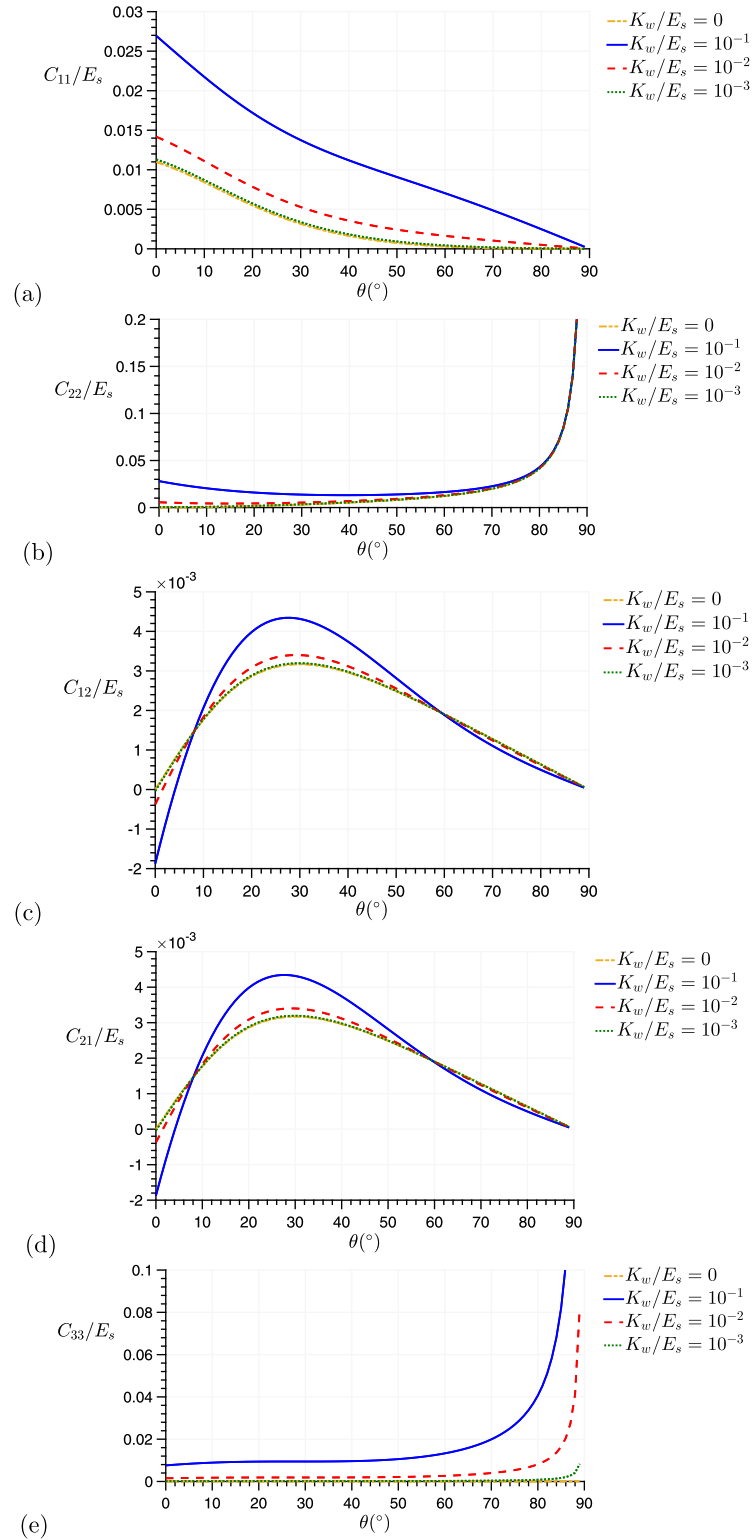
Fig. 8. The influence of K_w and θ in the effective stiffness constants in the case of $h/\ell = 0.01$: (a) C_{11}, (b) C_{22}, (c) C_{12}, (d) C_{21}, (e) C_{33}.

expected, for small values of θ the presence of the filling material does not stiffen the structure. Also, by comparing the curves corresponding to slender beams (Fig. 8(c) and (d)) and thick beams (Fig. 9(c) and (d)), it can be said that this peculiar behaviour is geometry-related. This result could be of interest in practical applications as a strategy to design a new more mechanically efficient material or to improve existing ones.

As in classical orthotropic materials, it emerges $C_{11} \neq C_{22}$ and $C_{12} = C_{21}$. Regardless the values of h/ℓ, only in the particular case $\theta = 30°$ the equivalence $C_{11} = C_{22}$ holds true. This, as expected, reveals the system isotropy.

5. Hierarchical extension

A hierarchical material can be defined as a material that contains structural elements which themselves have structure (Lakes, 1993;
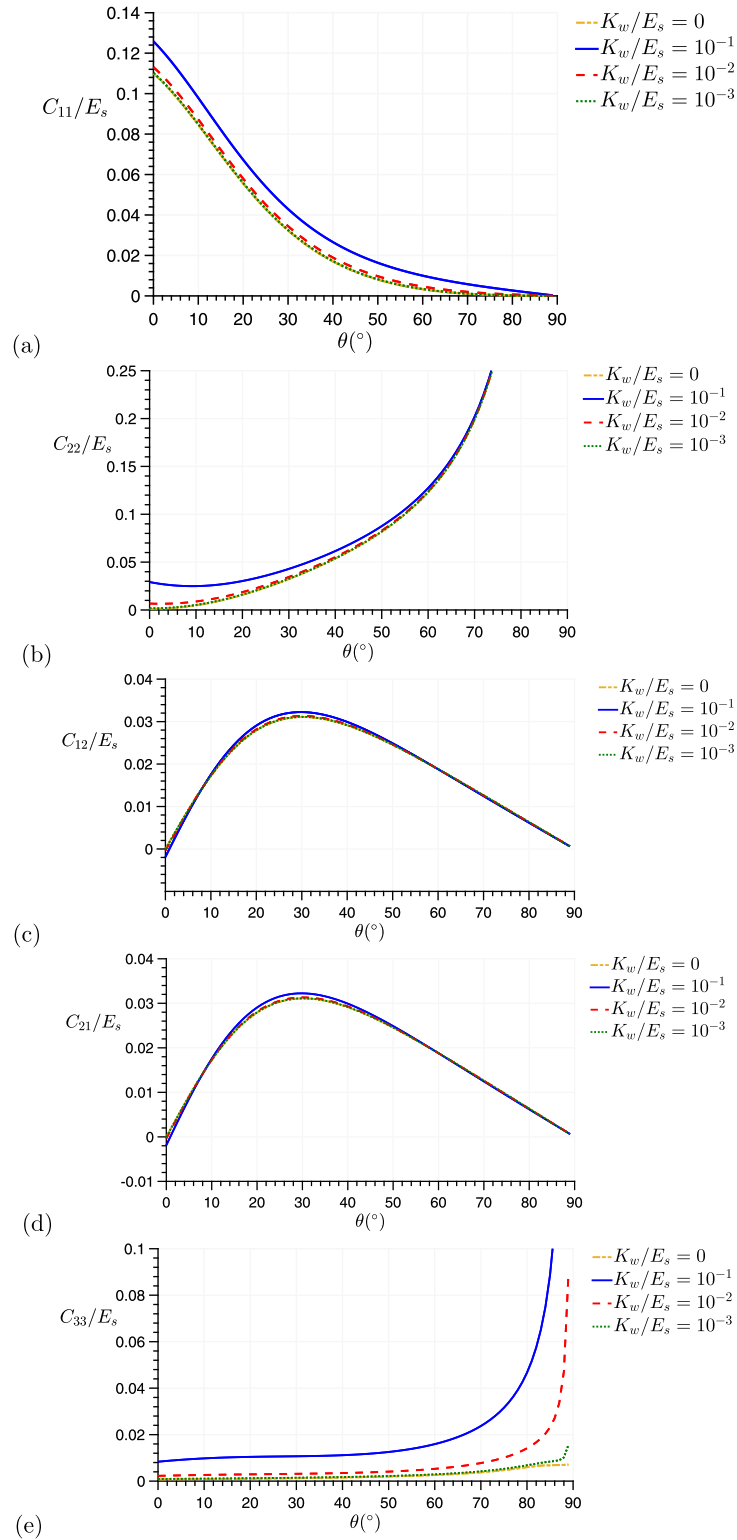
Fig. 9. The influence of K_w and θ in the effective stiffness constants in the case of $h/\ell = 0.1$: (a) C_{11}, (b) C_{22}, (c) C_{12}, (d) C_{21}, (e) C_{33}.

Ongaro et al., 2016a).

This work, in particular, deals with a hierarchical composite cellular material having n levels of hierarchy and an elongated hexagonal microstructure with filled cells at all levels (Fig. 10). Similarly to Section 2, the Euler–Bernoulli beam on Winkler foundation element represent the skeleton of the cells, the $(n-1)$th level. Again, the elastic springs are imagined to be anchored at the nodes of the lattice L_3, modelled as a sequence of Euler–Bernoulli beams much less stiff than

the principal ones (cf. Section 2.1).

5.1. Effective elastic constants

Let us focus on the nth level structure of Fig. 10. By assuming that the size of the microstructure of each cell wall, the $(n-1)$th level, is fine enough to be negligible with respect to the nth level, each cell arm can be treated as a continuum having the elastic moduli derived in
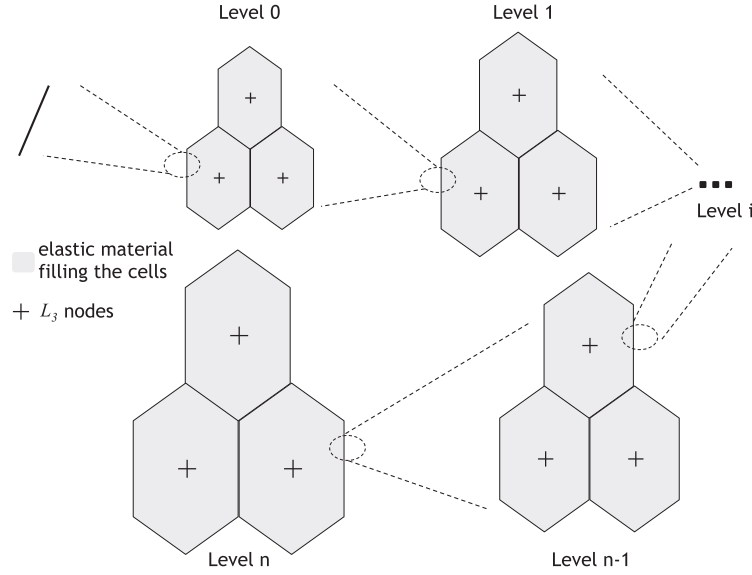
Fig. 10. The hierarchical composite cellular material.

Section 3.3. Consequently, the effective elastic constants of the *n*th level structure in the continuum form are

$$
\begin{aligned}
\check{E}_1 &= \frac{\check{c}(\check{K}_w \,\check{v}\,\check{c}^2((4\check{\lambda}^3 \check{f}_8 \,\check{E})/\check{v} + \check{f}_6 \,\check{K}_w(2\check{s}^2 + 1)) + 4\check{\lambda}\,\check{E}((104\check{\lambda}^3 \check{E}\check{f}_{10})/(\check{v}\check{f}_0) + \check{f}_7 \,\check{K}_w))}{4(\check{f}_9 \,\check{K}_w \,\check{v}(2\check{\lambda}^2 \check{c}^2 + 2\check{s}^2 + 1) + 104\check{\lambda}\check{f}_{10}\,\check{E}(\check{\lambda}^2 \check{c}^2 + \check{s}^2))} \\
&\quad + \frac{\check{\lambda}^2 \,\check{K}_w^2 \check{f}_5 \,\check{v}\,\check{c}^5}{2(\check{f}_9 \,\check{K}_w \,\check{v}(2\check{\lambda}^2 \check{c}^2 + 2\check{s}^2 + 1) + 104\check{\lambda}\check{f}_{10}\,\check{E}(\check{\lambda}^2 \check{c}^2 + \check{s}^2))}, \\[4pt]
\check{v}_{12} &= -\frac{\check{c}^2(\check{K}_w \,\check{v}\check{f}_2(2\check{\lambda}^2 \check{c}^2 + 2\check{s}^2 + 1) + 104\check{\lambda}(\check{\lambda}^2 - 1)\check{E}\check{f}_{11})}{\check{K}_w \,\check{v}\check{f}_4(2\check{\lambda}^2 \check{c}^2 + 2\check{s}^2 + 1) + 104\check{\lambda}\check{f}_0 \,\check{E}(\check{\lambda}^2\check{c}^2 + \check{s}^2)\check{f}_{11}/\check{s}}, \\[4pt]
\check{E}_2 &= \frac{4\check{\lambda}\,\check{E}((104\check{\lambda}^3 \,\check{E}\check{f}_{10})/(\check{v}\check{f}_0) + \check{f}_7 \,\check{K}_w) + \check{K}_w \,\check{c}^2(4\check{\lambda}^3 \,\check{E}\check{f}_8 + \check{K}_w \,\check{v}\check{f}_6(2\check{s}^2 + 1))}{4\check{f}_0 \,\check{c}(\check{K}_w \,\check{v}\check{f}_1(2\check{\lambda}^2 \check{c}^2 + 2\check{s}^2 + 1) + 104\check{\lambda}^3 \check{f}_3 \,\check{E}(\check{s}^2(3 + 2\check{c}^2) + 2\check{c}^4 + \check{c}^2))} \\
&\quad + \frac{\check{\lambda}^2 \,\check{K}_w^2 \check{v}\,\check{c}^3 \check{f}_6}{2\check{f}_0 (\check{K}_w \,\check{v}\check{f}_1(2\check{\lambda}^2 \check{c}^2 + 2\check{s}^2 + 1) + 104\check{\lambda}^3 \check{f}_3 \,\check{E}(\check{s}^2(3 + 2\check{c}^2) + 2\check{c}^4 + \check{c}^2))}, \\[4pt]
\check{v}_{21} &= -\frac{\check{K}_w \,\check{v}\check{f}_2(2\check{\lambda}^2 \check{c}^2 + 2\check{s}^2 + 1) + 104\check{\lambda}(\check{\lambda}^2 - 1)\check{f}_{11}\,\check{E}}{\check{K}_w \,\check{v}\check{f}_1(2\check{\lambda}^2 \check{c}^2 + 2\check{s}^2 + 1) + 104\check{\lambda}^3 \,\check{E}\check{f}_3(\check{s}^2(3 + 2\check{c}^2) + 2\check{c}^4 + \check{c}^2)}, \\[4pt]
\check{G} &= \frac{1}{416\check{f}_0 \,\check{c}}\left(\frac{104\check{\lambda}^3 \,\check{E}(\check{c}^2(2\check{\lambda}^2 + \check{f}_{13}) - 2\check{\lambda}^2 \check{s}\check{f}_0 + \check{f}_{12})}{\check{v}(\check{\lambda}^2(4\check{f}_8 \check{s} + 3) + 8\,\check{c}^2)} + \frac{\check{K}_w \check{f}_{11}}{\check{f}_{10}}\right),
\end{aligned}
$$

$$
\tag{57}
$$

with $\check{E}_1$, $\check{v}_{12}$ and $\check{E}_2$, $\check{v}_{21}$ Young's modulus and corresponding Poisson's ratio in the $\mathbf{e}_1$ and $\mathbf{e}_2$ direction, respectively, $\check{G}$ the shear modulus. In addition, $\check{\lambda} = \check{h}/\check{\ell}$, $\check{c}{:} = \cos\check{\theta}$, $\check{s}{:} = \sin\check{\theta}$ with $\check{h}$, $\check{\ell}$, $\check{\theta}$, in turn, the thickness, length and inclination of the cell walls (Fig. 10), $\check{K}_w$ the Winkler constant, $\check{v} = (1 - \check{v})$, $\check{E}$ and $\check{v}$ Young's modulus and Poisson's ratio of the beams in the longitudinal direction (Chen and Pugno, 2013; Pugno and Chen, 2011) obtained in Section 3.3. The polynomials $\check{f}_i = \check{f}_i(\cos\check{\theta}, \sin\check{\theta})$ are derived by substituting $\check{\theta}$ for θ into the expressions listed in Appendix B. It should be noted that the previous notation, $(\check{\cdot})$ for $(\cdot)^{(n)}$ and $(\check{\cdot})$ for $(\cdot)^{(n-1)}$, is introduced to simplify the relations and facilitate reading.

5.2. The stiffness-to-density ratio

The stiffness-to-density ratio takes the form

$$
\frac{\check{E}_1}{\check{\rho}} = \frac{\check{E}_1}{\check{a}\,\check{\rho}_f + \check{b}\,\check{\rho}}, \qquad
\frac{\check{E}_2}{\check{\rho}} = \frac{\check{E}_2}{\check{a}\,\check{\rho}_f + \check{b}\,\check{\rho}}, \qquad
\frac{\check{G}}{\check{\rho}} = \frac{\check{G}}{\check{a}\,\check{\rho}_f + \check{b}\,\check{\rho}},
\tag{58}
$$

with $\check{\rho}$ and $\check{E}_1$, $\check{E}_2$, $\check{G}$, in turn, the density and the effective elastic constants of the *n*th level structure previously defined. In particular, as explained in Appendix D, $\check{\rho}$ is given by

$$
\check{\rho} = \left(\frac{2\check{c}(1 + \check{s}) - 3\check{\lambda}}{2\check{c}(1 + \check{s})}\right)\check{\rho}_f + \left(\frac{3\check{\lambda}}{2\check{c}(1 + \check{s})}\right)\check{\rho} = \check{a}\,\check{\rho}_f + \check{b}\,\check{\rho},
\tag{59}
$$

where $\check{\rho}_f$ and $\check{\rho}$ are the density of the filling material, the first, and of the cell walls, the second, at level *n*.

5.3. Parametric analysis and optimal values

Based on the above formulation, this section aims at understanding how the microstructure's parameters affect the macroscopic elastic moduli in the case of structural hierarchy. The analysis involves a three-level hierarchical honeycomb having a elongated hexagonal microstructure with filled cells at all levels and such that the self-similar condition (Pugno and Chen, 2011)

$$
\lambda^{(i)} = \lambda, \qquad \theta^{(i)} = \theta, \qquad i = 1,\, 2,\, 3,
\tag{60}
$$

holds true. The hypothesis that the density of the filling material, $\rho_f^{(i)}$, is the same at all levels leads to

$$
\rho_f^{(i)} = \rho_f = \alpha\,\rho_s, \qquad i = 1,\, 2,\, 3,
\tag{61}
$$

with $\alpha = 0.4$, 0.2, 0.1, 0 for assumption. In addition, the lignified cell walls of the starting element, the level 0 in Fig. 10, have Young's modulus $E_s = 1$ GPa, Poisson's ratio $v_s = 0.3$, density $\rho_s = 1400$ kg/m^3 (Gibson and Ashby, 2001). The Winkler constant, derived in Appendix D, is expressed by

$$
K_w^{(i)} = K_w = \frac{4\sqrt{3}}{5}\alpha^3 E_s, \qquad i = 1,\, 2,\, 3.
\tag{62}
$$

As Fig. 11 shows, for fixed K_w the stiffness-to-density ratio, $E_1^{(3)}/\rho^{(3)}$, $E_2^{(3)}/\rho^{(3)}$, $G^{(3)}/\rho^{(3)}$, is strongly affected by the inclination of the cell walls θ, as in the not-hierarchical case. In particular, increasing the values of θ leads to an increase in $E_2^{(3)}/\rho^{(3)}$ and to a decrease in $E_1^{(3)}/\rho^{(3)}$. This is explained by the fact that the higher θ, the more elongated in the $\mathbf{e}_2$ direction will be the cell. Also, it emerges that the cell-filled configuration is generally stiffer than the hollow one ($K_w = 0$), especially in the case of high values of K_w ($10^{-1}E_s$, $10^{-2}E_s$). However, for high values of θ, Fig. 11(a) illustrates that the composite configuration with high values of K_w is not the best solution in terms of $E_1^{(3)}/\rho^{(3)}$. The reason is that, firstly, the macroscopic stiffness in the $\mathbf{e}_1$ direction is more and more smaller by increasing the cell walls' inclination. Secondly, filling the cells provides not only a stiffer material but also a higher value of the density. Regarding $E_2^{(3)}/\rho^{(3)}$, analogous considerations apply
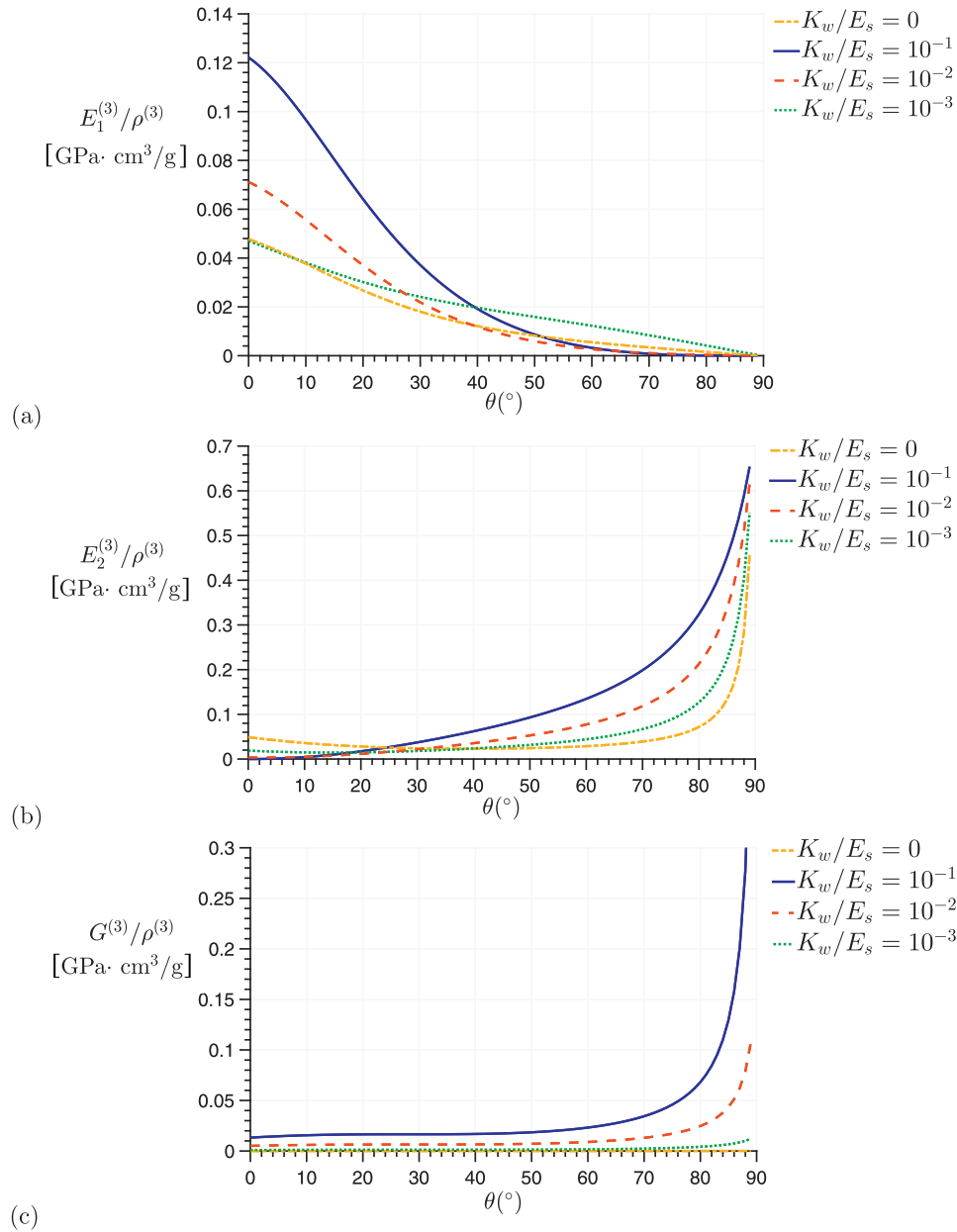
Fig. 11. The influence of K_w and θ in the stiffness-to-density ratios of a three-level hierarchical composite in the case of $h/\ell = 0.01$: (a) Young's modulus in the $\mathbf{e}_1$ direction, (b) Young's modulus in the $\mathbf{e}_2$ direction, (c) shear modulus.

(Fig. 11(b)). That is to say, high values of K_w leads to a stiffer material when $\theta > 24°$, since small values of θ result in a hierarchical configuration characterised by cells strongly elongated in the $\mathbf{e}_1$ direction and, consequently, by smaller values of $E_2^{(3)}$.

As expected, $E_1^{(3)}/\rho^{(3)} = E_2^{(3)}/\rho^{(3)}$ only in the case $\theta = 30°$.

Finally, in the cell-filled configuration, in contrast to the standard hierarchical material (Pugno and Chen, 2011; Bosia et al., 2012), increasing the number of hierarchical levels leads to an increase in the specific stiffness (Fig. 12) and an optimal number of levels also emerges.

In the practical context, these findings could suggest a method to obtain a stiffer composite material via structural hierarchy and could assist the designer in the selection of the geometric and mechanical characteristics of the microstructure.

6. Conclusions

Composite cellular materials have been credited with significantly improving the mechanical behaviour of hollow structures. However, in the literature a small number of analytical techniques has been proposed to predict the effective properties of filled cellular materials, especially in the case of not-regular microstructures.

This paper, inspired by the keel tissue of the ice plant *Delosperma nakurense*, deals with the analysis of a composite honeycomb composed by elongated cells filled with an elastic material. By modelling the composite hexagonal microstructure as a sequence of Euler–Bernoulli beams on Winkler foundation and by applying an energy-based technique, the constitutive equations and elastic moduli in the continuum approximation are derived. It emerges a strong influence of the cell walls' inclination and of the filler's stiffness on the effective elastic constants.
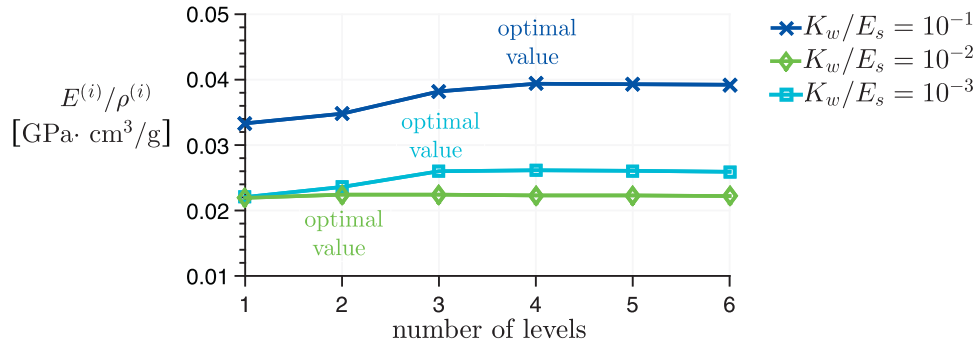
Fig. 12. Stiffness-to-density ratio vs levels of hierarchy, optimal value in the case of $h/\ell = 0.01$ and $\theta = 30°$.

The application of the theoretical model to the keel tissue of the ice plant, in conjunction with a comparison with the available data in the literature, reveals the validity of the proposed modelling approach. Despite the simplifications introduced to obtain a mathematically tractable problem, the present work could be useful to gain some insights into the mechanics of biological and bio-inspired structures.

The theory is also extended to the hierarchical configuration and a closed-form expression for the effective elastic moduli and specific stiffness is provided. From the parametric analysis developed, it emerges that increasing the hierarchical levels leads to an increase in the specific stiffness and an optimal number of levels also exists.

Acknowledgement

Appendix A

The elastic energy of the Euler–Bernoulli beam is the sum of three terms:

$$w^e = \frac{1}{2}(\mathbf{u}^e)^T \cdot \mathbf{k}_b^e \mathbf{u}^e + \frac{1}{2}(\Delta\mathbf{u}^{e,a})^T \cdot \mathbf{k}_{wf}^e \Delta\mathbf{u}^{e,a} + \frac{1}{2}(\Delta\mathbf{u}^{e,b})^T \cdot \mathbf{k}_{wf}^e \Delta\mathbf{u}^{e,b}. \tag{A.1}$$

The first,

$$\frac{1}{2}(\mathbf{u}^e)^T \cdot \mathbf{k}_b^e \mathbf{u}^e, \tag{A.2}$$

is related to the axial and bending deformations of the classical elastic beam, while the second and the third,

$$\frac{1}{2}(\Delta\mathbf{u}^{e,a})^T \cdot \mathbf{k}_{wf}^e \Delta\mathbf{u}^{e,a}, \qquad \frac{1}{2}(\Delta\mathbf{u}^{e,b})^T \cdot \mathbf{k}_{wf}^e \Delta\mathbf{u}^{e,b}, \tag{A.3}$$

are related to the Winkler foundation and, in particular, to the elongation of the springs a, the first, and of the springs b, the second (Fig. 14).

The elastic energy of the unit cell, W, derives from that of the beams composing the skeleton of the cells: 0–1, 0–2, 0–3. Also, imposing the balance of forces and moments in 0 and condensing the corresponding degrees of freedom, provides

$$W = W(\mathbf{u}_1, \mathbf{u}_2, \mathbf{u}_3, \Delta\mathbf{u}_1^a, \Delta\mathbf{u}_2^a, \Delta\mathbf{u}_3^a, \Delta\mathbf{u}_1^b, \Delta\mathbf{u}_2^b, \Delta\mathbf{u}_3^b). \tag{A.4}$$

Then, the assumption that in the limit $\ell \to 0$ the discrete variables $(\mathbf{u}_j, \varphi_j)$ can be written as

$$\mathbf{u}_j = \hat{\mathbf{u}}_0 + \nabla\hat{\mathbf{u}}\,\mathbf{b}_j$$
$$\varphi_j = \hat{\varphi}_0 + \nabla\hat{\varphi}\,\mathbf{b}_j, \qquad j = 1, 2, 3, \tag{A.5}$$

provides the continuum description of the discrete structure. The terms $\hat{\mathbf{u}}_0$ and $\hat{\varphi}_0$ are the values of $\hat{\mathbf{u}}(\cdot)$ and $\hat{\varphi}(\cdot)$ at the central point of the cell in the continuum description and in what follows, to simplify the notation, they will be denoted with $\hat{\mathbf{u}}$ and $\hat{\varphi}$. Finally, substituting (A.5) into (A.4) gives the strain energy of the unit cell as a function of the fields $\hat{\mathbf{u}}$ and $\hat{\varphi}$.

In particular, the aforementioned quantities are (Figs. 13–15):
– Beam 0–1
Discrete system

$$\Delta\mathbf{u}_1^a = \begin{bmatrix} \mathbf{u}_1 - \mathbf{u}_6 \\ \varphi_1 - \varphi_6 \end{bmatrix}, \qquad \Delta\mathbf{u}_1^b = \begin{bmatrix} \mathbf{u}_1 - \mathbf{u}_4 \\ \varphi_1 - \varphi_4 \end{bmatrix}. \tag{A.6}$$

In the continuum description,

$$\mathbf{u}_i = \hat{\mathbf{u}} + \nabla\hat{\mathbf{u}}\,\mathbf{b}_i, \qquad \varphi_i = \hat{\varphi} + \nabla\hat{\varphi}\,\mathbf{b}_i, \qquad i = 1, 6, 4, \tag{A.7}$$
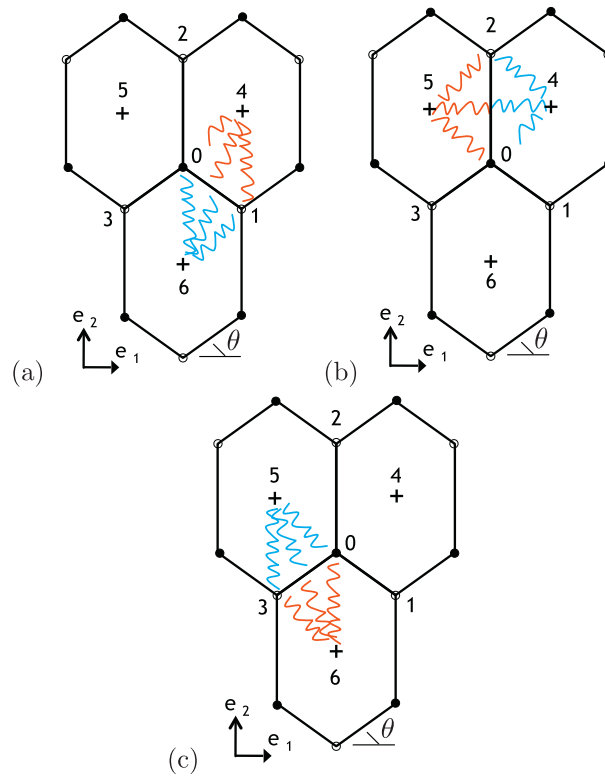
that, substituted in (A.6), lead to

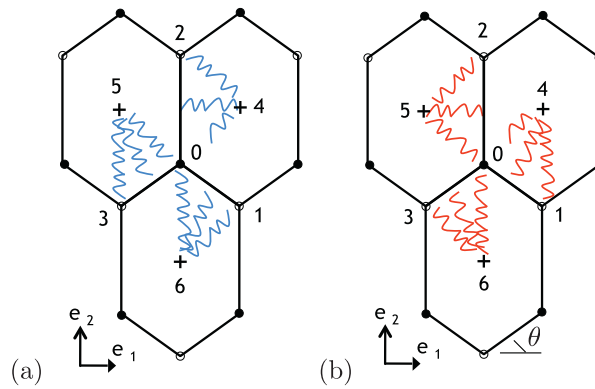**Fig. 13.** The triplet of elastic beams with focus on springs: (a) beam 0–1, (b) beam 0–2, (c) beam 0–3.

Fig. 14. The two sets of springs connecting the triplet of elastic beams: (a) springs a, (b) springs b.
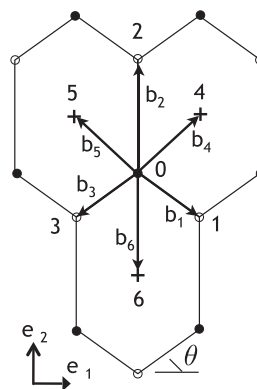

Fig. 15. The $\mathbf{b}_{fi}$ vectors.

$$\Delta \mathbf{u}_1^a = \begin{bmatrix} \nabla \hat{\mathbf{u}}\, \mathbf{b}_1 - \nabla \hat{\mathbf{u}}\, \mathbf{b}_6 \\ \nabla \hat{\varphi}\, \mathbf{b}_1 - \nabla \hat{\varphi}\, \mathbf{b}_6 \end{bmatrix}, \quad \Delta \mathbf{u}_1^b = \begin{bmatrix} \nabla \hat{\mathbf{u}}\, \mathbf{b}_1 - \nabla \hat{\mathbf{u}}\, \mathbf{b}_4 \\ \nabla \hat{\varphi}\, \mathbf{b}_1 - \nabla \hat{\varphi}\, \mathbf{b}_4 \end{bmatrix}. \tag{A.8}$$

– Beam 0–2

Discrete system

$$\Delta \mathbf{u}_2^a = \begin{bmatrix} \mathbf{u}_2 - \mathbf{u}_4 \\ \varphi_2 - \varphi_4 \end{bmatrix}, \quad \Delta \mathbf{u}_2^b = \begin{bmatrix} \mathbf{u}_2 - \mathbf{u}_5 \\ \varphi_2 - \varphi_5 \end{bmatrix}. \tag{A.9}$$

Continuum description

$$\mathbf{u}_i = \hat{\mathbf{u}} + \nabla \hat{\mathbf{u}}\, \mathbf{b}_i, \quad \varphi_i = \hat{\varphi} + \nabla \hat{\varphi}\, \mathbf{b}_i, \quad i = 2, 4, 5, \tag{A.10}$$

and

$$\Delta \mathbf{u}_2^a = \begin{bmatrix} \nabla \hat{\mathbf{u}}\, \mathbf{b}_2 - \nabla \hat{\mathbf{u}}\, \mathbf{b}_4 \\ \nabla \hat{\varphi}\, \mathbf{b}_2 - \nabla \hat{\varphi}\, \mathbf{b}_4 \end{bmatrix}, \quad \Delta \mathbf{u}_2^b = \begin{bmatrix} \nabla \hat{\mathbf{u}}\, \mathbf{b}_2 - \nabla \hat{\mathbf{u}}\, \mathbf{b}_5 \\ \nabla \hat{\varphi}\, \mathbf{b}_2 - \nabla \hat{\varphi}\, \mathbf{b}_5 \end{bmatrix}. \tag{A.11}$$

– Beam 0–3

Discrete system

$$\Delta \mathbf{u}_3^a = \begin{bmatrix} \mathbf{u}_3 - \mathbf{u}_5 \\ \varphi_3 - \varphi_5 \end{bmatrix}, \quad \Delta \mathbf{u}_3^b = \begin{bmatrix} \mathbf{u}_3 - \mathbf{u}_6 \\ \varphi_3 - \varphi_6 \end{bmatrix}. \tag{A.12}$$

Continuum description

$$\mathbf{u}_i = \hat{\mathbf{u}} + \nabla \hat{\mathbf{u}}\, \mathbf{b}_i, \quad \varphi_i = \hat{\varphi} + \nabla \hat{\varphi}\, \mathbf{b}_i, \quad i = 3, 5, 6, \tag{A.13}$$

and

$$\Delta \mathbf{u}_3^a = \begin{bmatrix} \nabla \hat{\mathbf{u}}\, \mathbf{b}_3 - \nabla \hat{\mathbf{u}}\, \mathbf{b}_5 \\ \nabla \hat{\varphi}\, \mathbf{b}_3 - \nabla \hat{\varphi}\, \mathbf{b}_5 \end{bmatrix}, \quad \Delta \mathbf{u}_3^b = \begin{bmatrix} \nabla \hat{\mathbf{u}}\, \mathbf{b}_3 - \nabla \hat{\mathbf{u}}\, \mathbf{b}_6 \\ \nabla \hat{\varphi}\, \mathbf{b}_3 - \nabla \hat{\varphi}\, \mathbf{b}_6 \end{bmatrix}. \tag{A.14}$$

Finally, the vectors $\mathbf{b}_i$ are (Fig. 15):

$$\begin{aligned} \mathbf{b}_1 &= \mathbf{l}_1 - \mathbf{s}, & \mathbf{b}_4 &= \mathbf{s}, \\ \mathbf{b}_2 &= \mathbf{l}_2 - \mathbf{s}, & \mathbf{b}_5 &= -\mathbf{s} - \mathbf{l}_1, \\ \mathbf{b}_3 &= -\mathbf{s}, & \mathbf{b}_6 &= (\mathbf{s} - \mathbf{l}_2)/2. \end{aligned} \tag{A.15}$$

Appendix B

B.1. Energy

The strain energy density in the continuum form defined in Section 3.1 is expressed by

$$
\begin{aligned}
w = {}& \frac{\varepsilon_{11}^2 C_\ell c\,(24c^4 D_\ell + 12 D_\ell s^2(1 + 2s^2) + c^2(C_\ell \ell^2 + 48 D_\ell s^2))}{2\ell(1 + s)(24c^2 D_\ell + C_\ell \ell^2(1 + 2s^2))} \\
&+ \frac{\varepsilon_{22}^2 C_\ell (1 + s)(12c^2 D_\ell + C_\ell \ell^2 s^2)}{2c\ell(24c^2 D_\ell + C_\ell \ell^2(1 + 2s^2))} + \frac{\varepsilon_{11}\varepsilon_{22} C_\ell c\,(-12 D_\ell + C_\ell \ell^2)s}{24c^2 D_\ell + C_\ell \ell^2(1 + 2s^2)} \\
&+ \frac{\varepsilon_{12}^2 3 D_\ell (4 C_\ell c^6 \ell^2 + 12 D_\ell s^2(1 + s)^2 + 4c^4(3 D_\ell + C_\ell \ell^2(1 + 2s(1 + s))))}{2c\ell^3(1 + s)(2 C_\ell c^2 \ell^2 + 3 D_\ell(3 + 4s(1 + s)))} \\
&+ \frac{\varepsilon_{12}^2 3 D_\ell (c^2(-24 D_\ell s(1 + s) + C_\ell \ell^2(3 + 4s(1 + s)(3 + s + s^2))))}{2c\ell^3(1 + s)(2 C_\ell c^2 \ell^2 + 3 D_\ell(3 + 4s(1 + s)))} \\
&+ \frac{9 D_\ell (\omega - \hat{\varphi})^2}{c\ell^3(3 + 4s(1 + s))} + \frac{\varepsilon_{11}\varepsilon_{22} K_w c\,(-1352 + s(9412 + s(1901 - 8s(8 + 1851s))))}{104(1 + s)(347 + 484s + 452s^2)} \\
&+ \frac{\varepsilon_{11}^2 K_w c\,(11518 + s(13520 + s(23761 + 24s(540 + 617s))))}{208(1 + s)(347 + 484s + 452s^2)} \\
&+ \frac{\varepsilon_{22}^2 K_w c\,(20280 + s(9464 + s(9721 + 8s(-1604 + 1851s))))}{208(1 + s)(347 + 484s + 452s^2)} \\
&+ \frac{\varepsilon_{12}^2 K_w (c^4(10969 + 8s(1958 + 1851s)) + 6c^2 s(4158 + s(2063 + 8(44 - 617s)s)))}{208c(1 + s)(347 + 484s + 452s^2)} \\
&+ \frac{\varepsilon_{12}^2 K_w s^2(35114 + s(22836 + s(21585 + 8s(-2222 + 1851s))))}{208c(1 + s)(347 + 484s + 452s^2)},
\end{aligned} \tag{B.1}
$$

with K_w the Winkler foundation constant, $C_\ell = \frac{E_s h}{1 - \nu_s^2}$ and $D_\ell = \frac{E_s h^3}{12(1 - \nu_s^2)}$, respectively, the tensile and bending stiffness (per unit width) of the beams, E_s, ν_s, h, ℓ and θ, in turn, Young's modulus, Poisson's ratio, thickness, length and inclination of the cell walls. Also, to simplify the notation, $c = \cos \theta$ and $s = \sin \theta$.

In the case of regular hexagonal microstructure, $\theta = 30°$, (B.1) takes the form

$$w = \frac{(\varepsilon_{11}^2 + \varepsilon_{22}^2)(C_\ell^2 \ell^4 + 36 D_\ell C_\ell \ell^2) + 2\varepsilon_{11}\varepsilon_{22}(C_\ell^2 \ell^4 - 12 D_\ell C_\ell \ell^2) + 96 D_\ell C_\ell \ell^2 \varepsilon_{12}^2}{4\sqrt{3}\,\ell^3 (12 D_\ell + C_\ell \ell^2)}$$
$$+ \frac{3 D_\ell (\omega - \hat{\varphi})^2}{\sqrt{3}\,\ell^3} + \frac{K_w (305(\varepsilon_{11}^2 + \varepsilon_{22}^2) + 544\,\varepsilon_{12}^2 + 66\,\varepsilon_{11}\varepsilon_{22})}{1664\sqrt{3}}. \tag{B.2}$$

B.2. Constitutive equations and elastic constants

The polynomial expressions $f_i = f_i(\cos\theta, \sin\theta)$ introduced in Section 3.2 are:

$$
\begin{aligned}
f_0 &= 1 + s, \\
f_1 &= 11518 + s(13520 + s(23761 + 24s(540 + 617s))), \\
f_2 &= s(s(8s(1851s + 8) - 1901) - 9412) + 1352, \\
f_3 &= 347 + 484s + 452s^2, \\
f_4 &= (s(s(8s(1851 - 1604) + 9721) + 9464) + 20280)c^2, \\
f_5 &= (((8(1851s - 2222)s + 21585)s + 22836)s + 35114)s^2 + (8(1851s + 1958)s + 10969)c^4 \\
&\quad + 6((8s(44 - 617s) + 2063)s + 4158)sc^2, \\
f_6 &= 25,688 + s(9464 + s(24,093 + 4s(581 + 8207s))), \\
f_7 &= s^2(1 + s)^2 f_1 + c^2 f_4 + 2c^2 s(1 + s)f_2, \\
f_8 &= 11,518 + 2f_4(1 + s^2) + 33,852s + 98,719s^2 \\
&\quad + 2s^3(53,046 + s(59,222 + s(9464 + s(9721 + 8s(-1604 + 1851s))))), \\
f_9 &= (1 + s)f_4, \qquad f_{10} = (1 + s)^3 f_4, \qquad f_{11} = s(s + 1)f_3, \\
f_{12} &= (8(s + 1)s + 4)c^4 + 4c^6, \qquad f_{13} = 4(s + 1)s(s + s^2 + 3) + 3,
\end{aligned} \tag{B.3}
$$

with $c = \cos\theta$ and $s = \sin\theta$.

In particular, for regular hexagonal microstructure, $\theta = 30°$,

$$
\begin{aligned}
&f_0 = 3/2, \quad f_1 = 107,055/4, \quad f_2 = -11,583/4, \quad f_3 = 702, \quad f_4 = 321,165/16, \\
&f_5 = 35,802, \quad f_6 = 77,571/2, \quad f_7 = 53,703/2, \quad f_8 = 249,561/2, \quad f_9 = 963,495/32, \\
&f_{10} = 9477/4, \quad f_{11} = 1053/2, \quad f_{12} = 117/16, \quad f_{13} = 57/4.
\end{aligned} \tag{B.4}
$$

Accordingly, the constitutive equations and elastic moduli of Sections 3.2 and 3.3 take the form:

$$
\begin{aligned}
\sigma_{11} = \sigma_{11}^{sym} &= \frac{(C_\ell^2 \ell^2 + 36 D_\ell C_\ell)\varepsilon_{11} + (C_\ell^2 \ell^2 - 12 D_\ell C_\ell)\varepsilon_{22}}{2\sqrt{3}\,\ell(12 D_\ell + C_\ell \ell^2)} + \frac{K_w(305\varepsilon_{11} + 33\varepsilon_{22})}{832\sqrt{3}}, \\
\sigma_{22} = \sigma_{22}^{sym} &= \frac{(C_\ell^2 \ell^2 + 36 D_\ell C_\ell)\varepsilon_{22} + (C_\ell^2 \ell^2 - 12 D_\ell C_\ell)\varepsilon_{11}}{2\sqrt{3}\,\ell(12 D_\ell + C_\ell \ell^2)} + \frac{K_w(305\varepsilon_{22} + 33\varepsilon_{11})}{832\sqrt{3}}, \\
\sigma_{12}^{sym} = \sigma_{21}^{sym} &= \frac{48 D_\ell C_\ell \varepsilon_{12}}{2\sqrt{3}\,\ell(12 D_\ell + C_\ell \ell^2)} + \frac{17 K_w \varepsilon_{12}}{52\sqrt{3}}, \\
\sigma_{12}^{skw} = -\sigma_{21}^{skw} &= \frac{\sqrt{3}\,D_\ell(\omega - \hat{\varphi})}{\ell^3}, \\
\sigma_{12} = \sigma_{12}^{sym} + \sigma_{12}^{skw}, &\quad \sigma_{21} = \sigma_{21}^{sym} + \sigma_{21}^{skw},
\end{aligned} \tag{B.5}
$$

and

$$
\begin{aligned}
E_1^* = E_2^* \equiv E^* &= \frac{(13 K_w(1 - \nu_s^2) + 32\lambda E_s)(17(1 + \lambda^2)K_w(1 - \nu_s^2) + 104\lambda^3 E_s)}{2\sqrt{3}(1 - \nu_s^2)(305(1 + \lambda^2)K_w(1 - \nu_s^2) + 416(\lambda + 3\lambda^3)E_s)}, \\
\nu_{12}^* = \nu_{21}^* \equiv \nu^* &= \frac{33(1 + \lambda^2)K_w(1 - \nu_s^2) - 416\lambda(\lambda^2 - 1)E_s}{305(1 + \lambda^2)K_w(1 - \nu_s^2) + 416\lambda(1 + 3\lambda^2)E_s}, \\
G^* &= \frac{17(1 + \lambda^2)K_w(1 - \nu_s^2) + 104\lambda^3 E_s}{104\sqrt{3}(1 + \lambda^2)(1 - \nu_s^2)}.
\end{aligned} \tag{B.6}
$$

Appendix C

As stated, an energetic equivalence provides a suitable relation between the Winkler foundation constant of the present work, K_w, and the hydrostatic pressure p of Guiducci et al. (2014).

First of all, let us focus on a single cell and let us consider its elastic energy, W_c, obtained by summing the contribution of the walls, W_w, and of the filling material, W_f:

$$W_c = W_w + W_f. \tag{C.1}$$

In particular,

$$W_c = \begin{cases} W_{c,Winkler} = W_{w,beams} + W_{f,Winkler} & \text{Winkler model} \\ W_{c,pressurized\ cell} = W_{w,walls} + W_{pressure} & \text{pressurized cell,} \end{cases} \tag{C.2}$$
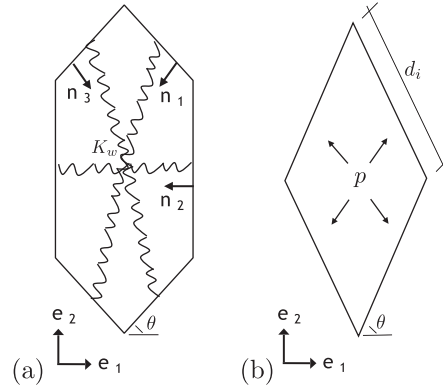
Fig. 16. Practical application to the keel tissue of the ice plant. Equivalence between (a) the Winkler foundation model and (b) the pressurized cell (Guiducci et al., 2014).

with $W_{w,\,beams}$, $W_{f,\,Winkler}$ and $W_{w,\,walls}$, $W_{pressure}$, in turn, the elastic energies of the cell walls and of the filling material in the case of Winkler foundation model, Fig. 16(a), and pressurized cell (Guiducci et al., 2014), Fig. 16(b). By assuming

$$W_{w,beams} \equiv W_{w,walls}, \tag{C.3}$$

the energetic equivalence

$$W_{c,Winkler} \equiv W_{c,pressurized\ cell} \tag{C.4}$$

takes the form

$$W_{f,Winkler} \equiv W_{pressure}. \tag{C.5}$$

The first term, $W_{f,\,Winkler}$ is the sum of the elastic energies of the three series of springs in the directions $\mathbf{n}_1$, $\mathbf{n}_2$, $\mathbf{n}_3$:

$$W_{f,\,Winkler} = \left(\sum_{i=1}^{3} \frac{1}{2} \mathbf{\Delta U}_i^T \cdot \mathbf{K}_w \mathbf{\Delta U}_i \right) b, \tag{C.6}$$

where $\mathbf{\Delta U}_i$ is the elongation of the springs in the $\mathbf{n}_i$ direction, b the width,

$$\mathbf{K}_w = \begin{bmatrix} K_w & 0 \\ 0 & K_w \end{bmatrix} \tag{C.7}$$

the stiffness matrix of the elastic foundation, K_w the Winkler constant. Also, $W_{pressure}$ is related to the change in the volume of the cell and its expression, given in Guiducci et al. (2014), is

$$W_{pressure} = -p \frac{V - V_0}{V_0} = -p((1 + \varepsilon_{11})(1 + \varepsilon_{22}) - 1)b, \tag{C.8}$$

with p the inner pressure, $V = V(p)$ and $V_0 = V(p = 0)$, respectively, the volume of the cell in the deformed and undeformed configuration, b the width. From classical continuum mechanics, the strains $\varepsilon_{ij} = \varepsilon_{ij}(p)$ take the form

$$\varepsilon_{ij}(p) = \mathbf{n}_i^T \epsilon_f(p) \mathbf{n}_i = \frac{\Delta d_i}{d_i}, \qquad i = 1, 2, 3, \tag{C.9}$$

with Δd_i the elongation in the $\mathbf{n}_i$ direction, $\epsilon_f(p)$ the infinitesimal strain tensor,

$$d_1 = d_3 = \ell \sqrt{2 + 2 \sin \theta(p)}, \qquad d_2 = 2\ell \cos \theta(p), \tag{C.10}$$

and $\theta(p)$ the inclination of the cell walls in the deformed configuration (Fig. 16). In addition, the assumption

$$\Delta U_i = \Delta d_i, \qquad i = 1, 2, 3 \tag{C.11}$$

provides, in view of (C.9),

$$\mathbf{n}_i^T \epsilon_f(p) \mathbf{n}_i = \frac{\Delta U_i}{d_i}, \qquad i = 1, 2, 3, \tag{C.12}$$

leading to

$$\Delta U_i = (\mathbf{n}_i^T \epsilon_f(p) \mathbf{n}_i) d_i, \qquad i = 1, 2, 3. \tag{C.13}$$

Substituting (C.13) into (C.6) and taking into account (C.5), gives

$$\sum_{i=1}^{3} \frac{1}{2} d_i (\mathbf{n}_i^T \epsilon_f(p) \mathbf{n}_i)^T \mathbf{K}_w \mathbf{n}_i (\mathbf{n}_i^T \epsilon_f(p) \mathbf{n}_i)^T d_i = p((1 + \varepsilon_{11}(p))(1 + \varepsilon_{22}(p)) - 1). \tag{C.14}$$

From standard mathematical manipulations, it follows

$$K_w = \frac{p(-(1 + \varepsilon_{11}(p))(1 + \varepsilon_{22}(p)) + 1)2\cos\theta(p)(1 + \sin\theta(p))}{\sqrt{2 + 2\sin\theta(p)}\,(\sin\theta(p)^2\varepsilon_{11}(p) + \cos\theta(p)^2\varepsilon_{22}(p))^2 + \cos\theta(p)\varepsilon_{22}(p)^2},$$

(C.15)

being

$$\varepsilon_{11}(p) = \frac{\sin\theta(p)}{\sin\theta_0} - 1, \qquad \varepsilon_{22}(p) = \frac{\cos\theta(p)}{\cos\theta_0} - 1$$

(C.16)

obtained from classical continuum mechanics and simple geometrical considerations. In the above relations, $\theta_0 = \theta(p = 0)$ stands for the inclination of the cell walls in the undeformed configuration and its approximated value, 75°, is given in Guiducci et al. (2014). By considering this and inserting (C.16) into (C.15), it emerges

$$K_w(p) = \frac{\sqrt{2}\,p\left(-\dfrac{8\sin\theta(p)\cos\theta(p)}{17} + 1\right)\cos\theta(p)\sqrt{1 + \sin\theta(p)}}{\left(\dfrac{4\sin^3\theta(p)}{6 + \sqrt{2}} + \dfrac{4\cos^3\theta(p)}{6 - \sqrt{2}} - 1\right)^2 + \cos\theta(p)\left(\dfrac{4\cos\theta(p)}{6 - \sqrt{2}} - 1\right)^2},$$

(C.17)

where the values of $\theta(p)$ are derived from Guiducci et al. (2014).

Appendix D

D.1.   Density

Let us focus on the 0th order level structure in Fig. 11. From the rule of mixtures, the density of this composite configuration, $\rho^{(0)}$, is given by

$$\rho^{(0)} = f^{(0)}\rho_f^{(0)} + (1 - f^{(0)})\rho_s,$$

(D.1)

with $f^{(0)} = V_f^{(0)}/V_{tot}^{(0)}$ the porosity, $V_f^{(0)}$ and $V_{tot}^{(0)}$, in turn, the volume of the filling material and of the entire cell, ρ_s and $\rho_f^{(0)}$ the density of the cell walls, the first, and of the filler, the second. In particular,

$$f^{(0)} = \frac{A_f^{(0)}b}{A_{tot}^{(0)}b} = \frac{2\cos\theta^{(0)}(1 + \sin\theta^{(0)}) - 3\lambda^{(0)}}{2\cos\theta^{(0)}(1 + \sin\theta^{(0)})},$$

(D.2)

where $A_{tot}^{(0)}$ and $A_f^{(0)}$ are, on order, the total area of the cell and of the filling material, b the width, $\lambda^{(0)} = h^{(0)}/\ell^{(0)}$ the ratio between the thickness and length of the walls. Accordingly,

$$\rho^{(0)} = \left(\frac{2\cos\theta^{(0)}(1 + \sin\theta^{(0)}) - 3\lambda^{(0)}}{2\cos\theta^{(0)}(1 + \sin\theta^{(0)})}\right)\rho_f^{(0)} + \left(\frac{3\lambda^{(0)}}{2\cos\theta^{(0)}(1 + \sin\theta^{(0)})}\right)\rho_s$$

(D.3)

or, to simplify the notation,

$$\rho^{(0)} = a^{(0)}\rho_f^{(0)} + b^{(0)}\rho_s,$$

(D.4)

with

$$a^{(0)} = \frac{2\cos\theta^{(0)}(1 + \sin\theta^{(0)}) - 3\lambda^{(0)}}{2\cos\theta^{(0)}(1 + \sin\theta^{(0)})}, \qquad b^{(0)} = \frac{3\lambda^{(0)}}{2\cos\theta^{(0)}(1 + \sin\theta^{(0)})}.$$

(D.5)

Regarding the density of the first level structure ($n = 1$), $\rho^{(1)}$, let us assume that the length of scale of the cell walls' microstructure is much smaller than the cell wall itself. So, as done in Section 5.1, a continuum having density $\rho^{(0)}$ approximates each cell arm. As a consequence,

$$\rho^{(1)} = a^{(1)}\rho_f^{(1)} + b^{(1)}\rho^{(0)}$$

(D.6)

where $\rho_f^{(1)}$ is the density of the filling material, $a^{(1)}$, $b^{(1)}$ are derived by substituting $\theta^{(1)}$ and $\lambda^{(1)} = h^{(1)}/\ell^{(1)}$ for $\theta^{(0)}$ and $\lambda^{(0)}$.

Finally, analogous calculations provide the density in the case on n levels of hierarchy:

$$\rho^{(n)} = a^{(n)}\rho_f^{(n)} + b^{(n)}\rho^{(n-1)},$$

(D.7)

with $\rho_f^{(n)}$ and $\rho^{(n-1)}$, in turn, the density of the filler and of the cell walls, $a^{(n)}$ and $b^{(n)}$ obtained as before.

D.2.   Winkler foundation constant as a function of the filler's Young's modulus

In Section 5.3, the hypothesis that the density of the filling material, $\rho_f^{(i)}$, is the same at all levels provides

$$\rho_f^{(i)} = \rho_f = \alpha\rho_s, \qquad i = 1, 2, 3,$$

(D.8)

with α a positive constant depending on the material inside the cells. For simplicity, let us assume that the filler is a standard cellular material with hexagonal microstructure, as commonly happens in nature (Gibson and Ashby, 2001). Thus, the classical relations (Gibson and Ashby, 2001)

$$\frac{\rho_f^{(i)}}{\rho_{s,f}} = \frac{2}{\sqrt{3}}\lambda_f^{(i)}, \qquad \frac{E_f^{(i)}}{E_{s,f}} = \frac{4}{\sqrt{3}}(\lambda_f^{(i)})^3, \qquad i = 1, 2, 3$$

(D.9)

provide its (effective) Young's modulus, $E_f^{(i)}$, and density, $\rho_f^{(i)}$, as a function of the cell walls' properties, i.e., the thinness ratio, $\lambda_f^{(i)}$, the density, $\rho_{s,f}$, and Young's modulus, $E_{s,f}$.

By taking into account the energetic equivalence in Ongaro et al. (2016b),

$$K_w^{(i)} = \frac{8}{5\sqrt{3}} E_f^{(i)}, \qquad i = 1, 2, 3,$$
(D.10)

together with the assumption

$$\rho_{s,f} = \rho_s, \qquad E_{s,f} = E_s,$$
(D.11)

simple mathematical manipulations give

$$K_w^{(i)} = \frac{4\sqrt{3}}{5} E_s \left(\frac{\rho_f^{(i)}}{\rho_s} \right)^3, \qquad i = 1, 2, 3,$$
(D.12)

a suitable relation between the Winkler constant, $K_w^{(i)}$, and the filler's density. Finally, in view of (D.8),

$$K_w^{(i)} = K_w = \frac{4\sqrt{3}}{5} \alpha^3 E_s, \qquad i = 1, 2, 3.$$
(D.13)

In particular, four values of α are considered: 0.4, 0.2, 0.1, 0, leading to $K_w = 10^{-1}E_s$, $10^{-2}E_s$, $10^{-3}E_s$, 0, respectively.

References

Ajdari, A., Jahromi, B.H., Papadopoulos, J., Hashemi, H.N., Vaziri, A., 2012. Hierarchical honeycombs with tailorable properties. Int. J. Solids Struct. 49, 1413–1419.

Altenbach, H., Oechsner, A., 2010. Cellular and Porous Materials in Structures and Processes. CISM.

Barthelat, F., Mirkhalaf, M., 2013. The quest for stiff, strong and tough hybrid materials: an exhaustive exploration. J. R. Soc. Interface 10, 1–11.

Bitzer, T., 1994. Honeycomb marine applications. J. Reinf. Plast. Compos. 13, 355–360.

Bosia, F., Abdalrahman, T., Pugno, N.M., 2012. Investigating the role of hierarchy on the strength of composite materials: evidence of a crucial synergy between hierarchy and material mixing. Nanoscale 4, 1200–1207.

Burgardt, B., Cartraud, P., 1999. Continuum modeling of beam-like lattice trusses using averaging methods. Comput. Struct. 73, 267–279.

Burlayenko, V.N., Sadowski, T., 2010. Effective elastic properties of foam-filled honeycomb cores of sandwich panels. Compos. Struct. 92, 2890–2900.

Chen, C.N., 1998. Solution of beam on elastic foundation by DQEM. J. Eng. Mech. ASCE 124, 1381–1384.

Chen, J.Y., Huang, Y., Ortiz, M., 1998. Fracture analysis of cellular materials: a strain gradient model. J. Mech. Phys. Solids 46 (5), 789–828.

Chen, Q., Pugno, N.M., 2013. Biomimetic mechanisms of natural hierarchical materials: a review. J. Mech. Behav. Biomed. Mater. 19, 3–33.

Davini, C., Ongaro, F., 2011. A homogenized model for honeycomb cellular materials. J. Elast. 104, 205–226.

Dinev, D., 2012. Analytical solution of beam on elastic foundation by singularity functions. Eng. Mech. 19, 381–392.

D'Mello, R.J., Waas, A.M., 2013. In-plane crush response and energy absorption of circular cell honeycomb filled with elastomer. Compos. Struct. 106, 491–501.

Dos Reis, F., Ganghoffer, J.F., 2010. Discrete homogenization of architectured materials: implementation of the method in a simulation tool for the systematic prediction of their effective elastic properties. Tech. Mech. 30, 85–109.

Dos Reis, F., Ganghoffer, J.F., 2012. Construction of micropolar continua from the asymptotic homogenization of beam lattices. Comput. Struct. 112–113, 354–363.

Eisenberger, M., Yankelevsky, D.Z., 1985. Exact stiffness matrix for beams on elastic foundation. Comput. Struct. 21, 1335–1359.

Fan, H.L., Jin, F.N., Fang, D.N., 2008. Mechanical properties of hierarchical cellular materials. part i: analysis. Compos. Sci. Technol. 68, 3380–3387.

Fenner, R.T., 1996. Finite Element Methods for Engineers. Imperial College Press.

Fratzl, P., 2007. Biomimetic materials research: what can we really learn from nature's structural materials? J. R. Soc. Interface 4, 637–642.

Fratzl, P., Weinkamer, R., 2007. Nature's hierarchical materials. Mater. Sci. 52, 1263–1334.

Gao, H., 2010. Learning from nature about principles of hierarchical materials. Proceedings of the 2010 IEEE International NanoElectronics Conference (INEC).

Georget, D.M.R., Smith, A.C., Waldron, K.W., 2003. Modelling of carrot tissue as a fluid-filled foam. J. Mater. Sci. 38, 1933–1938.

Gibson, L.J., 1989. Modelling the mechanical behavior of cellular materials. Mat. Sci. Eng. A110, 1–36.

Gibson, L.J., 2012. The hierarchical structure and mechanics of plant materials. J. R. Soc. Interface 9, 2749–2766.

Gibson, L.J., Ashby, M.F., 2001. Cellular solids. Structure and Properties. Cambridge University Press.

Gibson, L.J., Ashby, M.F., Harley, B.A., 2010. Cellular Materials in Nature and Medicine. Cambridge University Press.

Gibson, L.J., Ashby, M.F., Schajer, G.S., Robertson, C.I., 1982. The mechanics of two-dimensional cellular materials. Proc. R. Soc. Lond. A 382, 25–42.

Guiducci, L., Fratzl, P., Brechet, Y.J.M., Dunlop, J.W., 2014. Pressurized honeycombs as soft-actuators: a theoretical study. J. R. Soc. Interface 11, 1–12.

Haghpanah, B., Papadopoulos, J., Mousanezhad, D., Hashemi, H.N., 2014. Buckling of regular, chiral and hierarchical honeycombs under a general macroscopic stress state. Proc. R. Soc. A 470, 8–56.

Harrington, M.J., Razghandi, K., Ditsch, F., Guiducci, L., Rueggeberg, M., Dunlop, J.W.C., Fratzl, P., Neinhuis, C., Burgert, I., 2011. Origami-like unfolding of hydro-actuated ice plant seed capsules. Nat. Commun. 2 (337), 1–7.

Hosur, V., Bhavikatti, S.S., 1996. Influence lines for bending moments in beams on elastic foundations. Comput. Struct. 58, 1225–1231.

Janco, R., 2010. Solution methods for beam and frames on elastic foundation using the finite element method. Proceedings of the 2010 International Scientific Conference on Mechanical Structures and Foundation Engineering, MSFE.

Karkon, M., Karkon, H., 2016. New element formulation for free vibration analysis of Timoshenko beam on Pasternak elastic foundation. Asian J. Civil Eng. 17 (4), 427–442.

Kumar, R.S., McDowell, D.L., 2004. Generalized continuum modeling of 2-D periodic cellular solids. Int. J. Solids Struct. 41, 7399–7422.

Kuo, Y.H., Lee, S.Y., 1994. Deflection of nonuniform beams resting on a nonlinear elastic foundation. Comput. Struct. 51, 513–519.

Lakes, R., 1993. Materials with structural hierarchy. Nature 361, 511–515.

Lockyer, S., 1932. Seed dispersal from hygroscopic mesembryanthemum fruits, berger-anthus scapigerus, schw., and dorotheanthus bellidiformis, N. E. Br., with a note on carpanthea pomeridiana, N.E. Br. Ann. Bot. 46, 323–342.

Mattheck, C., Kubler, H., 1995. The Internal Optimization of Trees. Springer Verlag, Berlin.

Meyers, M.A., Chen, P.Y., Lin, A.Y.M., Seki, Y., 2008. Biological materials: structure and mechanical properties. Prog. Mater. Sci. 53, 1–206.

Mihai, L.A., Alayyash, K., Goriely, A., 2015. Paws, pads and plants: the enhanced elasticity of cell-filled load-bearing structures. Proc. R. Soc. A 471, 1–20.

Niklas, K.J., 1989. Mechanical behavior of plant tissues as inferred from the theory of pressurized cellular solids. Am. J. Bot. 76, 929–937.

Niklas, K.J., 1992. Plant Biomechanics: An Engineering Approach to Plant Form and Function. University of Chicago Press.

Ongaro, F., Barbieri, E., Pugno, N.M., 2016. The in-plane elastic properties of hierarchical composite cellular materials: synergy of hierarchy, material heterogeneity and cell topologies at different levels. Mech. Mater. 103, 135–147.

Ongaro, F., De Falco, P., Barbieri, E., Pugno, N.M., 2016. Mechanics of filled cellular materials. Mech. Mater. 97, 26–47.

Pan, N., 2014. Exploring the significance of structural hierarchy in material systems – a review. Appl. Phys. Rev. 1, 1–31.

Pugno, N.M., Chen, Q., 2011. In-plane elastic properties of hierarchical cellular solids. Phys. Eng. 10, 3026–3031.

Razaqpur, A.G., Shah, K.R., 1991. Exact analysis of beams on two-parameter elastic foundations. Int. J. Solids Struct. 27, 435–454.

Sanchez, C., Arribart, H., Giraud Guille, M.M., 2005. Biomimetism and bioinspiration as tools for the design of innovative materials and systems. Nat. Mater. 4, 277–288.

Sen, Y.L., Huei, Y.K., Yee, H.K., 1990. Elastic static deflection of a non-uniform Bernoulli–Euler beam with general elastic end restraints. Comput. Struct. 36, 91–97.

Taylor, C.M., Smith, C.W., Miller, W., Evans, K.E., 2011. The effects of hierarchy on the in-plane elastic properties of honeycombs. Int. J. Solids Struct. 48, 1330–1339.

Thompson, R.W., Matthews, F.L., 1995. Load attachments for honeycomb panels in racing cars. Mater. Des. 16, 131–150.

Tsiatas, G.C., 2014. A new efficient method to evaluate exact stiffness and mass matrices of non-uniform beams resting on an elastic foundation. Arch. Appl. Mech. 84, 615–623.

Van Liedekerke, P., Ghysels, P., Tijkens, E., Samaey, G., Smeedts, B., Roose, D., Ramon,

H., 2010. A particle-based model to simulate the micromechanics of single-plant parenchyma cells and aggregates. Phys. Biol. 7, 1–13.

Wang, X.L., Stronge, W.J., 1999. Micropolar theory of two-dimensional stresses in elastic honeycomb. Proc. R. Soc. Lond. A 455, 2091–2116.

Warner, M., Thiel, B.L., Donald, A.M., 2000. The elasticity and failure of fluid-filled cellular solids: theory and experiment. PNAS 97 (4), 1370–1375.

Warren, W.E., Byskov, E., 2002. Three-fold symmetry restrictions on two-dimensional micropolar materials. Eur. J. Mech. A/Solids 21, 779–792.

Wilson, S., 1990. A new face of aerospace honeycomb. Mater. Des. 11, 323–326.

Wu, N., Pitts, M.J., 1999. Development and validation of a finite element model of an apple fruit cell. Postharvest Biol. Technol. 16, 1–8.

Zhu, H.X., Melrose, J.R., 2003. A mechanics model for the compression of plant and vegetative tissues. J. Theor. Biol. 221, 89–101.